Research Article

Au-O-MWCNTs and TiO$_2$-O-MWCNTs as Efficient Nanocarriers for Dexamethasone: Adsorption Isotherms and Kinetic Studies

Maryam Haghighi [ID] and Azadeh Khoshfetrat

Department of Chemistry, Faculty of Physics and Chemistry, Alzahra University, Tehran, Iran

Correspondence should be addressed to Maryam Haghighi; m.haghighi@alzahra.ac.ir

In this research, the fabrication of drug delivery systems based on oxidized multiwall carbon nanotubes (O-MWCNTs) was studied. Herein, TiO$_2$ and Au were conjugated with O-MWCNTs to prepare efficient nanocarriers for dexamethasone (dex). The samples were characterized by Fourier transform infrared (FTIR), scanning electron microscopy (SEM), and X-ray diffraction (XRD). In addition, dex loading was studied using adsorption isotherms including Langmuir, Freundlich, Temkin, and Dubinin–Radushkevich. The results show that dex adsorption agreed well with the Freundlich isotherm. Increasing the TiO$_2$ to O-MWCNT ratio from (1 : 4) to (1 : 2) can improve the adsorption capacity from 290 mg $\cdot$ g^{-1} to 320 320 mg $\cdot$ g^{-1}. The increasing Au amount increases the adsorption capacity from 437.78 mg $\cdot$ g^{-1} (SA1) to maximum 476.19 mg $\cdot$ g^{-1} (SA6). The maximum equilibrium binding energy A_T (1.67 L $\cdot$ mg^{-1}) was obtained for SA2, and SA7 shows high binding strength between dex and the nanoadsorbent. Carbon nanotubes (CNTs) show good affinity with high loading capabilities for dexamethasone adsorption. The synthesized TiO$_2$-O-MWCNTs:1/2 with the maximum removal percent (80%) was proposed as an appropriate nanocarrier for dexamethasone. Pseudo-first order, pseudo-second order, Elovich, and intraparticle diffusion models were investigated for all synthesized drug nanocarriers. According to regression coefficients, experimental data are in good agreement with the pseudo-second order model for all adsorbents except O-MWCNT/CTAB. Experimental results revealed that the Elovich model could account for the O-MWCNT/CTAB adsorbent.

1. Introduction

Dexamethasone is a type of steroid hormone and a strong combinatorial derived of the glucocorticoid hydrocortisone [1]. The chemical name of dex is 9-fluoro-11,17,21-trihydroxy-16-methylpregna-1,4-diene-3,20-dione with molecular formula C$_{22}$H$_{29}$FO$_5$. Dex is extensively used to treat many diseases such as allergy, inflammation, osteoporosis, and some skin diseases [2, 3]. The prolonged use of dex sometimes shows some harmful side effects, particularly during pregnancy. The dosage injection or oral administration of dex is a key factor in treatment [4].

Targeted drug delivery has been employed to overcome the adverse effects using different nanostructures. Nanomaterials can be served as the commercially invented structures to improve drug efficacy [4, 5]. Over the past decade, several types of nanomaterials have been successfully synthesized for the use against pathogens, and a variety of nanoplatforms, including nanofibers, nanosized micelles, nanomagnetic particles, and liposomes, have been emerged to promote the efficiency of drug delivery systems (DDSs) [6–10]. These nanomaterials have new opportunities and prospects for targeted and adjusted drug delivery and controlled therapy [11]. In addition, using nanoDDSs can prevent the destruction of healthy tissues and drug resistance [12].

The nanocarriers can be classified to organic, inorganic, and hybrid inorganic/organic categories. Biomolecules such as dendrimers and liposomes have been used for targeted drug delivery to cancer cells or tissues [13, 14]. Biopolymers

such as collagen, polylactic acid, albumin, gelatin, cellulose, starch, and hyaluronic acid have been employed as exciting alternatives. Chitosan is a well-known and biodegradable polymer and can serve as a high potency carrier for loading, delivery, and release of paclitaxel, betamethasone, and tetracycline into human bodies [15, 16]. One important issue in the design of the bioderived polymers is achieving uniform and highly pure structures with similar molecular weight, chain length, viscosity, and number of functional groups. One strategy to enhance the drug efficacy is to use synthetic polymers in the design of DDSs with predictable properties. Moreover, more nanoplatforms have been formulated using inorganic nanocarriers including metal oxides [17], MOFs [18, 19], and carbon-based materials [20, 21]. These inorganic nanomaterials showed distinct properties, and are often cheap, highly stable, biocompatible, controllable, and adjustable.

Mesoporous silica nanoparticles have gained more attention in metal ion removal such as Pb and Cu in waste water treatment [22, 23]. Its large surface area, specific shape of pores, and tunable pore size offer excellent storage capacity. The mesoporous silica can be combined with different ligands to prepare innovative nanocomposites. The potency of these mesoporous silica to physical and chemical adsorption is affected by operating conditions. The targeted delivery of poor water-soluble drugs can be possible by using mesoporous materials such as mesoporous silica and mesoporous carbon. Scattered size distribution and difficulty in stable-colloidal suspension are the remarkable drawbacks of silica-based DDSs [24]. According to literature survey, some modifications were carried out to enhance the biocompatibility and targeted drug delivery of silica nanocomposites. Recently, mesoporous silica has been combined with carbon nanotubes (CNTs) to improve the drug delivery capabilities [25].

Among numerous nanovehicles with the aim of targeted drug delivery, carbon nanotubes were extensively studied [26–29]. The extraordinary potencies of CNTs, including high elasticity [30], high thermal and electrical conductivity [31, 32], remarkable optical properties [33], and extreme aspect ratio, made them suitable for a wide range of applications such as energy storage systems, composites, sensors [34, 35], molecule transportation and protein carriers [36], tissue engineering, and photothermal therapy [37–41]. In light of the enormous advantages of CNTs in biological applications, the carbon-based nanomedicine has been considered by many multidisciplinary researchers.

The CNTs were reported in 1991 for the first time by the Japanese physicist Sumio Iijima [42]. He synthesized CNTs using an arc-burned graphite probe (CVD method) that showed enormous characteristics and were used in many industrial and scientific applications. Carbon nanotubes can form a single layer of graphene, which is called single-wall carbon nanotubes (SWCNTs), or concentric graphene sheets, which is called multiwall carbon nanotubes (MWCNT). CNTs can be synthesized in different sizes (diameter is variable from 10 to 200 nm and different lengths) and different grades of purity, which is dependent on the synthesis method and operating conditions such as temperature and pressure.

MWCNTs show encouraging biological features compared to other nanostructures that have been studied over the past decade. The lower price, higher efficiency, the ability to load more cargo of drug, high chemical resistance, physical steadiness, and less cytotoxic properties of MWCNTs compared to the SWCNTs made them more appropriate for DDS systems. Moreover, the remarkable aspect ratio of carbon nanotubes provides the physical or chemical adsorption of biomolecules onto CNTs. The special needle-shape of CNTs allows the efficient intramembrane permeability during endocytosis and improves enhanced permeability and retention (EPR) effect [26]. They also show the antioxidant nature that can protect drug molecules. The covalent/noncovalent functionalization of CNTs makes them more efficient for drug loading and controlled release. The blood-brain barrier (BBB) is the main obstacle in brain tumor treatment. In addition, CNTs equipped with chemotherapy drugs can overcome the blood-brain barrier and facilitate the drug delivery to brain tissue [43]. Some earlier studies represent the use of MWCNTs for targeted delivery and controlled release of anticancer drugs such as doxorubicin (DOX) and paclitaxel [44, 45]. The folic acid grafted MWCNTs were employed successfully for targeted delivery of doxorubicin [46]. The CNTs have been also employed to prepare a wide range of biological scaffoldings in tissue engineering. Moreover, CNT is a suitable candidate for the adsorption of ciprofloxacin hydrochloride from aqueous solutions. The results show that ciprofloxacin hydrochloride can be adsorbed by MWCNTs successfully. Moreover, the kinetic study and isotherm models were investigated comprehensively [47].

However, apart from these distinguished properties, insolubility of MWCNTs is an important challenge in DDS development (led to a slight cytotoxicity). Due to the intratublar van der Waals forces, the roll sheets of CNTs tend to aggregate together, which shows their amphiphobic nature. The difficulty is enhanced due to the poor dispersibility and solubility of MWCNTs in most solvents. On the other hand, the intrinsic poor solubility of MWCNTs is a serious obstacle in the commercialization of these nanocarriers [48–50]. Therefore, MWCNTs as a drug carrier tend to deposit in the blood circulation system or different organs. Different strategies have been proposed to overcome the hydrophobic nature of CNTs and increase the stability of the solutions [51]. The tuning of MWCNT structure by functionalization using a hydrophilic group improves dispersibility and reduces cytotoxicity. For instance, carbon nanotubes are simply functionalized by carboxylic groups of strong acids, which increases drug adsorption. It was found that carboxylic groups show hydrophilic property and can create defects on the CNT side walls and get attached to these generated defects. It has been postulated that the COOH groups can be coupled with the open ends of CNTs and functionalize them; they can cut and shorten the tubes chemically and make them appropriate for intratube drug loading without deposition and toxicological side effects to the human body. Moreover, the biocompatibility of carbon nanotubes escalates and, therefore, a large diversity of molecules such as proteins, nucleic acids, and drug

molecules can be attached to the oxidized MWCNTs [17]. Drug molecules attach to the MWCNT surface via covalent or noncovalent bonds and can be delivered to the intended organ, and are released and absorbed into the human body. The functionalized MWCNTs can be degraded enzymatically and excreted via the kidney at the end of the drug delivery process. Therefore, the CNTs functionalized with COOH groups render many active sites for drug loading. The drug molecules can be trapped in the O-MWCNTs for providing an efficient drug delivery system.

The main goal of this work is to prepare and study the novel nanocomposites based on multiwall carbon nanotubes as suitable carriers for dexamethasone. Both covalent functionalization of sidewalls and intrinsic defects were considered in this research. Metal oxides show great potential in the design of the DDSs due to their inherent mechanical and chemical stability. In order to increase the adsorption capacity and overcome the limitations of using of MWCNTs, metal oxides/MWCNT nanocomposites have been constructed and studied in this research. This could be a solution to increase the drug uptake on the surface of MWCNTs to provide targeted delivery. Different nanoparticles were dispersed and immobilized on the surface of O-MWCNTs. In this endeavor, TiO_2 and Au were applied as good alternatives for drug nanocarrier fabrication due to their high adsorption capacity. Drug release characteristics are dependent on the method of drug loading onto or into a nanocarrier. Moreover, the drug loading and pharmacokinetic behavior of these nanodrug carriers were further investigated comprehensively in order to control drug adsorption and drug delivery to target cells. Meanwhile, the adsorption isotherms and kinetic models were studied in this research. The results show that the prepared nanocomposites with high surface area can adsorb dex molecules effectively.

2. Materials and Methods

2.1. Materials. All chemicals used are commercially available as received. MWCNTs (95%, $10\,\mu m$ length, and 10–30 nm diameter) and the colloidal mixture of gold nanoparticles (1000 ppm) were purchased from Nanosav Company. Dex as an anti-inflammatory drug was obtained from Osvah Company. Titanium dioxide was purchased from Nanosany Corporation. Cetyltrimethylammonium bromide (CTAB) and polyethylene glycol with MW = 4000 (PEG 4000) were of analytical-reagent grade and prepared by Merck Company. The solutions in this study were all prepared with double distilled water.

2.2. Instruments. A Bruker FTIR model Tensor 27 spectrometer (KBr disks, 500–4000 cm^{-1}) was applied for recording the IR spectra. SEM images were determined using a scanning electron microscope (model EM 3200, kyky), and an X-ray diffractometer (cobalt anode, wavelength of 1.7889°A, Cu Kα1 radiation, 40 kV, 40 mA) was used for obtaining XRD patterns. UV-vis spectra were obtained using a UV spectrophotometer (model Perkin Elmer lambda 35, 190 nm–1100 nm).

2.3. Functionalization of MWCNTs. 0.2 g of MWCNTs were added to 100 ml of H_2SO_4 (98%) and HNO_3 (69%) mixture (V/V = 3 : 1) and stirred with a magnetic stirrer (rpm = 250) for 2 h at room temperature, then mixed using an ultrasonic device for 1 h. The prepared solution was centrifuged and washed with purified water several times until the pH of the mixture was adjusted to neutral. The precipitate was dried in an oven at 80℃ for 24 h. The pretreated MWCNTs, which were the so-called O-MWCNTs, were used for adsorbent fabrication.

2.4. Adsorbent Preparation. In this study, the effect of surfactants (CTAB and PEG 4000) on the dex loading efficiency was investigated. In this regard, O-MWCNTs (0.006 g), CTAB (0.006 g), and 100 mL double distilled water were stirred in an ultrasonic bath for 45 min. The prepared nanotubes were centrifuged and washed several times with deionized water and absolute ethanol. The produced precipitate was dried at 80℃ in an oven for 4 h to obtain SA1 nanocomposite. In a next attempt, O-MWCNTs (0.006 g) and PEG 4000 (0.006 g) were taken, and the aforementioned procedure was carried out to prepare SA2.

Metals have been routinely applied in the structure of different adsorbents, which can improve the adsorption performance. Herein, Au and TiO_2 were added to the adsorbent structure. First, different amounts of Au were immobilized on the surface of the O-MWCNTs to determine the optimum value. 0.05 g of O-MWCNTs and 0.5 mL of colloidal Au solution (1000 ppm) were dispersed in 20 mL of purified water using a magnetic stirrer for 1 h, followed by redispersion in an ultrasonic bath for 1 h again. The mixture was centrifuged and washed with double distilled water and absolute ethanol several times and then dried at 80℃ for 4 h again (SA3 sample). The experiment was utilized for different values of the Au solution (1000 ppm) as 1 mL, 1.5 mL, and 2 mL. The samples were called SA4, SA5, and SA6, respectively. In the next step, titanium dioxide was used to improve the adsorption capacity of carbon nanotubes. 0.05 g of O-MWCNTs and 0.0125 g of TiO_2 (anatase phase, with average size 10–25 nm) were dispersed in 20 ml double distilled water to produce SA7. The same procedure was applied to 0.01 g of TiO_2 and 0.02 g of O-MWCNTs to prepare SA8 sample. The specifications of materials and obtained adsorbents are summarized in Tables 1 and 2.

2.5. Analysis of Dex Samples. New nanoplatforms were designed to maximize drug concentration into targeted sites with minimum drug loading dosage. In order to overcome the drug toxicity problems, its dosage should be controlled by taking advantages of drug delivery nanosystems. Dex loading on the samples, which were reported in Table 2, were compared together in this research. The oxidized samples were subjected to the dex adsorption process under a similar procedure to measure the drug uptake. Dex (2 mg/8 mL) was immersed in double distilled water. Specific amounts of different nanocarriers were added to this solution under ultrasonic stirring. Finally, the suspension was centrifuged,

TABLE 1: Sample table.

Chemical name	Source	Initial mole fraction purity	Purification method	Final mole fraction purity	Analysis method
MWCNTs	Nanosav company	0.95	None	—	—
Gold nanoparticles	Nanosav company	—	None	—	—
Dexamethasone	Osvah company	—	None	—	—
CTAB[a]	Merck	—	None	—	—
PEG[b]	Merck	—	None	—	—
TiO$_2$	Nanosany corporation	—	None	—	—

[a]Cetyltrimethylammonium bromide, [b]polyethylene glycol.

TABLE 2: Synthesized adsorbents for dex loading.

Entry	Adsorbent	Metal	Sample name
1	O-MWCNT/CTAB		SA1
2	O-MWCNT/PEG		SA2
3	Au-O-MWCNT	0.5 mL of colloidal Au solution	SA3
4	Au-O-MWCNT	1 mL of colloidal Au solution	SA4
5	Au-O-MWCNT	1.5 mL of colloidal Au solution	SA5
6	Au-O-MWCNT	2 mL of colloidal Au solution	SA6
7	TiO$_2$-O-MWCNT	0.05 g of O-MWCNTs and 0.0125 g of TiO$_2$	SA7
8	TiO$_2$-O-MWCNT	0.01 g of TiO$_2$ and 0.02 g of O-MWCNTs	SA8

and the precipitate was washed several times with distilled water and absolute ethanol. Dex content in upper clear solution was quantitatively analyzed by UV-vis spectrophotometry at 238 nm to calculate the drug uptake. The UV spectrum of dex solution is shown in Figure 1 with maximum absorptivity at λ_{max} = 238 nm.

All experiments were performed in diluted solution so that the Beer–Lambert law is valid. The linear relationship between the concentration of adsorbed pieces and absorbance can be written as follows:

$$A = \varepsilon \cdot b \cdot c, \tag{1}$$

where ε is the molar absorptivity coefficient ($M^{-1} \cdot cm^{-1}$), b is the path length (width of cell is 1 cm), C is the molar concentration, and ε is the slope of the calibration curve. Four solutions with a low molar concentration of dex were prepared (4e-6, 8e-6, 12e-5, and 16e-5), and the absorbance versus molar concentration of these samples is depicted in Figure 2. The experimental data were fitted to a straight line, and the concentrations of unknown samples were calculated using this calibration curve.

2.6. Batch Experiments for Optimization, Kinetic and Isotherm Studies

2.6.1. Batch Studies for Optimum Temperature.
According to the literature, adsorption is a function of various parameters such as temperature, pH, and contact time [52]. Since acidic or basic pH may affect drug structure, dex loading was studied at neutral pH to avoid drug destruction or any other side effects. To define the proper adsorption temperature, 0.024 g of O-MWCNTs and 0.024 g of CTAB were added to 100 ml double distilled water in a 500 mL beaker and mixed together in an ultrasonic bath for 45 min. Furthermore, 400 ml of dex solution (6.2e-5 M) was slowly added to the
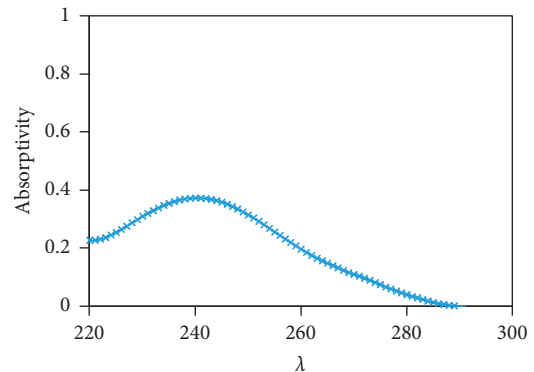

FIGURE 1: UV spectrum of dex.

beaker and mixed for 30 min under sonication. Adsorption experiments were conducted at different temperatures; 293 K, 298 K, 303 K, and 308 K for 30 min at neutral pH. After dex loading, the adsorbent was separated from the suspension via the centrifugal method. The dex concentration in effluent solution was analyzed using the UV-vis adsorption spectrum according to a prepared calibration curve. The removal percent of dex and adsorption capacity at the equilibrium state q_e (mg $\cdot$ g^{-1}) were calculated by equations (2) and (3), respectively [23],

$$\%\text{Removal} = \frac{(C_0 - C_e)}{C_0} \times 100, \tag{2}$$

$$q_e = \frac{(C_0 - C_e) \cdot V}{m}, \tag{3}$$

where C_0 (mg $\cdot$ L^{-1}) and C_e (mg $\cdot$ L^{-1}) are the initial and equilibrium concentrations of dex, respectively; V (L) is the volume of the drug solution; and m (g) is the weight of the
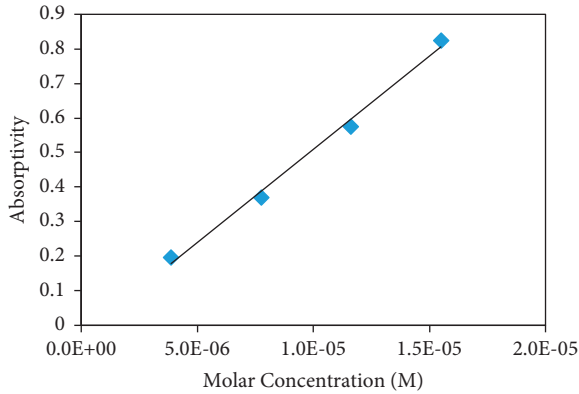
FIGURE 2: Calibration curve for dex solution.

adsorbent. The desired temperature can be identified with regard to the maximum adsorption capacity, although dex thermal stability ought to be considered. Similar experiments conducted on other nanoadsorbents showed the same results for optimum temperature. This may be due to the fact that the O-MWCNTs were applied as the main part of all synthesized nanoadsorbents. On the other hand, the temperature adjusted for O-MWCNTs (as the support of nanocarriers) can be generalized to all samples.

2.6.2. Batch Studies for Surfactant Selection.
Coupling the functional groups with adsorbents during drug loading or nanocarrier formulation are widely used to improve the solubility and nanocarrier stabilization. As a part of this work, the effectiveness of PEG and CTAB on dex loading was examined. 0.006 g of SA1 was added to 100 mL of 2.32e-5 M of dex solution (pH = 7.3) and mixed in an ultrasonic bath at a defined temperature of 303 K. The amount of dex concentration in the remaining solution was measured at different time intervals (5, 15, 25, 35, 50, 65, 80, 95, and 110 min). Dex adsorption capacity (q_t) at any given time was plotted as a function of contact time by the following equation:

$$q_t = \frac{(C_0 - C_t) \cdot V}{m}, \tag{4}$$

where $C_t \, (\mathrm{mg \cdot L^{-1}})$ is the concentration of adsorbed dex at any given time. All experiments were conducted several times, and the average values were applied for this research. Furthermore, the same adsorption experiments were conducted for SA2 in the presence of an appropriate surfactant (which was identified regarding higher drug loading values).

2.6.3. Batch Studies for Contact Time, Kinetic and Isotherm Models.
The kinetic studies were performed in a 250 mL beaker containing 0.006 g of SA3 or other adsorbents (SA4, SA5, SA6, SA7, and SA8), 0.006 g of desired surfactant, and 100 mL of double distilled water at optimum temperature and neutral pH. After mixing in an ultrasonic bath for 45 min, 100 mL of 2.32e-5 M of dex solution was dissolved in this solution. Mixing was continued, and drug adsorption capacity at defined time intervals were analyzed for each case. In this regard, the optimum contact time was further

investigated with equilibrium adsorption capacity. It is necessary to mention that, since the surfactant can help in drug encapsulation or conjugation, the proposed surfactant should be added to the synthesized nanoplatforms during the drug loading process simultaneously.

Furthermore, in order to investigate the isotherms, batch experiments were examined for different dosages of dex at equilibrium contact time, neutral pH, and optimum temperature. 0.006 g of SA1 was dissolved in drug solutions of different concentrations 3.1e-5, 2.71e-5, 1.94e-5, and 1.55e-5 at laboratory temperature and at pH = 7.3 and agitated during the optimum contact time. After reaction completion, the adsorbent was separated by the centrifugal process, and the dex concentration was quantitatively analyzed using UV. Similar experiments were conducted for other adsorbents at proper contact time.

2.7. Kinetic Models.
Kinetic studies provide novel methods to design selective adsorbents for other drugs with innovative sorption properties. Moreover, the experimental results were applied to understand the optimum contact time and maximum adsorption capacity, aiming at controlling the complexity of the adsorption systems. The kinetics of dex loading were studied by four well-known models, pseudo-first order, pseudo-second order, Elovich, and intraparticle diffusion models, to obtain new insights into dex adsorption [52–57].

In the pseudo-first-order model, the difference in equilibrium uptake and time dependent uptake is expressed as a linear function of the adsorption time. The pseudo-first-order kinetic model is given as follows [58–60]:

$$\ln(q_e - q_t) = \ln q_e - k_1 t, \tag{5}$$

where $k_1 \, (\mathrm{min^{-1}})$ is the adsorption rate constant of the pseudo-first-order model.

The pseudo-second-order model can be applied in adsorption processes, whereas chemisorption is the rate-controlling step. The linear equation of the pseudo-second-order kinetic model evaluates the adsorption rate as follows [61]:

$$\frac{t}{q_t} = \frac{1}{k_2 q_e^2} + \frac{1}{q_e} t, \tag{6}$$

where $k_2 \, (\mathrm{g \cdot mg^{-1} \cdot min^{-1}})$ is the rate constant of the pseudo-second-order kinetic model.

The Elovich model is usually used to predict the adsorption rate where the chemisorption is carried out in heterogeneous systems. The linear form of the Elovich kinetic model can be expressed as follows [62]:

$$q_t = \frac{1}{\beta} \ln(\alpha\beta) + \frac{1}{\beta} \ln(t), \tag{7}$$

where $\alpha \, (\mathrm{mg \cdot g^{-1} \cdot min^{-1}})$ is the initial adsorption rate, and $\beta \, (\mathrm{g \cdot mg^{-1}})$ is the Elovich adsorption constant.

The kinetic model of adsorption depends on the physical properties of the adsorbent and chemical properties of the sorption process. In general, diffusion was carried out at

different stages, comprising of mass transfer from the aqueous solution to the surface of the solid adsorbent through a diffusion boundary layer, penetration to the tortuous path, and subsequently the intraparticle diffusion of species. The process continued to achieve the equilibrium state between absorption and desorption rates. It is important to identify the controlling step of adsorption kinetics aimed toward understanding the effective parameters of the adsorption rate. In this regard, the intraparticle kinetic model was taken into consideration to investigate the diffusion mechanism instead of the pseudo-first and second order equations. Weber–Morris model was applied to intraparticle diffusion of dex in this research to define the rate determining and slowest step of the diffusion mechanism [63, 64]. The Weber–Morris kinetic model was illustrated as follows:

$$q_t = k_i t^{1/2} + C, \tag{8}$$

where $k_i \, (\mathrm{mg} \cdot \mathrm{g}^{-1} \cdot \mathrm{min}^{-1/2})$ is the rate constant of diffusion and C is the intercept of the plot.

2.8. Isotherm Models. The amount of the adsorbed drug on the solid surface is a function of its concentration in the bulk of the solution at the equilibrium state. Multiple isotherms have been developed to describe the adsorption behavior on the adsorbent. Insights obtained from the isotherms have been used to predict the equilibrium adsorption capacity, which plays a key role in the design of new adsorbents for industrial applications. In this research, various isotherms have been employed for the O-MWCNT-based adsorbents. The isotherms have been developed with regard to the complexity of the interactions between the atoms and molecules in the sorptive-sorbent system. All experimental data have been measured under well-defined conditions at the equilibrium state to indicate the mechanism of physisorption or chemisorption. In most cases, the theoretical results are in line with experimental data without significant deviation.

In this investigation, the adsorption system was analyzed using four most proposed isotherms, Langmuir, Freundlich, Temkin, and Dubinin–Radushkevich. The Langmuir model describes the monolayer adsorption by a linear equation as follows [22, 65]:

$$\frac{C_e}{q_e} = \frac{1}{K_L q_{\max}} + \frac{C_e}{q_{\max}}, \tag{9}$$

where $q_e \, (\mathrm{mg} \cdot \mathrm{g}^{-1})$ is the amount of adsorbate at the equilibrium state, $q_{\max} \, (\mathrm{mg} \cdot \mathrm{g}^{-1})$ is the maximum adsorption capacity, C_e is the adsorbate concentration at the equilibrium state, and $K_L \, (\mathrm{L} \cdot \mathrm{mg}^{-1})$ is the Langmuir constant. The C_e/q_e is plotted versus C_e as a straight line with intercept $1/K_L q_{\max}$. The separation factor R_L is a main criterion for adsorption evaluation that can be calculated as follows:

$$R_L = \frac{1}{1 + K_L C_0}. \tag{10}$$

The separation factor at all examined initial concentrations should be determined using the Langmuir constant.

Whether the R_L values are lower than unity, the adsorption process is favorable and valid [58]. The Freundlich isotherm is normally represented by the nonuniform adsorption of the species on heterogeneous systems. Equation (11) represents the Freundlich isotherm as follows [66, 67]:

$$Ln \, q_e = Ln \, K_F + \frac{1}{n} Ln \, C_e, \tag{11}$$

where $K_F \, (\mathrm{mg} \cdot \mathrm{g}^{-1} \, (\mathrm{L} \cdot \mathrm{mg})^{-1/n})$ and n are the Freundlich constants, which are calculated using the Freundlich isotherm plot. Lnq_e is depicted versus LnC_e, and the slope and intercept of this straight line are calculated. Furthermore, the linear Temkin isotherm can be expressed by the following formula [68]:

$$q_e = B_T Ln \, A_T + B_T \, Ln \, C_e,$$
$$B_T = \frac{RT}{b}, \tag{12}$$

where $b \, (\mathrm{J/mol})$ and $A_T \, (\mathrm{L/g})$ are the equilibrium binding constants, b is a function of heat of sorption, A_T is the Temkin equilibrium isotherm constant, whereas R is the gas constant, and T is the absolute temperature. q_e is plotted against LnC_e as a straight line, and the constants of Temkin isotherm are measured, which can be used for result prediction. If the heat of adsorption decreases with an increment of the surface coverage, Temkin isotherm governs the adsorption system.

The Dubinin–Radushkevich isotherm was developed with regard to the Guassian energy distribution onto the heterogeneous surface of the adsorbent with a linear formula as follows [62]:

$$\ln q_e = \ln q_D - K_{DR} \times \varepsilon^2, \tag{13}$$

where $q_D \, (\mathrm{mg} \cdot \mathrm{g}^{-1})$ describes the theoretical saturation capacity, $K_{DR} \, (\mathrm{mol}^2 \cdot \mathrm{J}^2)$ is the Dubinin–Radushkevich constant related to the mean free energy of adsorption, and ε is the Polanyi potential, which is expressed according to the equilibrium data as follows:

$$\varepsilon = RT \, \ln \left[1 + \frac{1}{C_e} \right]. \tag{14}$$

The mean energy of adsorption can be calculated by the following equation:

$$E = \frac{1}{\sqrt{2K_{DR}}}. \tag{15}$$

3. Results and Discussion

3.1. Characterization of Prepared Nanocomposites. The synthesized samples were thoroughly characterized via FTIR, SEM images, and XRD patterns. In order to identify the mechanism of dex adsorption, the FTIR spectra of various nanocarriers after dex loading were recorded, and the results were compared to the FTIR spectrum of O-MWCNTs before dex loading. Figure 3 shows the FTIR spectra of O-MWCNTs before dex loading and
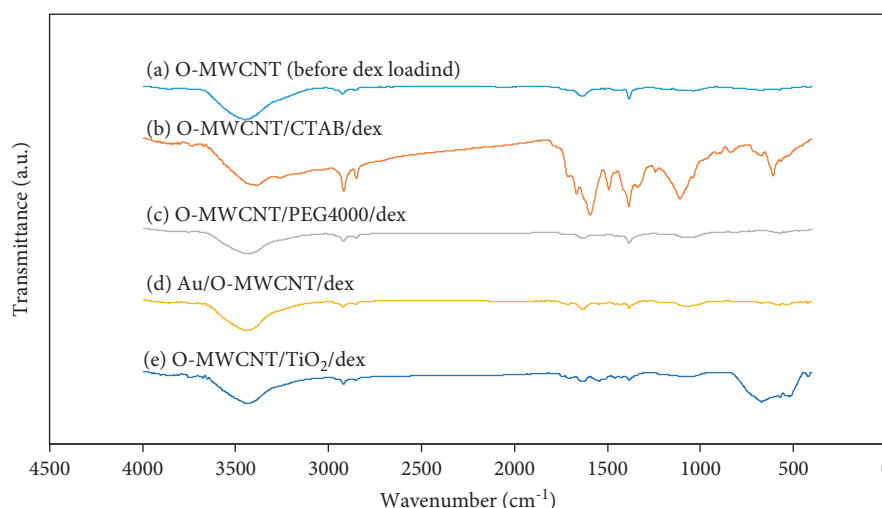
FIGURE 3: FTIR spectra of different nanocarriers. (a) O-MWCNTs (before dex loading), (b) O-MWCNT/CTAB/dex, (c) O-MWCNT/PEG4000/dex, (d) Au-O-MWCNT/dex: SA6, and (e) TiO$_2$-O-MWCNT/dex: SA7.

O-MWCNT/CTAB (SA1), O-MWCNT/PEG (SA2), Au-O-MWCNT (SA6), and TiO$_2$-O-MWCNT (SA7) after dex adsorption onto these nanocarriers. The recorded spectrum in Figure 3(a) corresponds to the O-MWCNT before dex adsorption. The observed bands at $3449 \, cm^{-1}$ and $1429 \, cm^{-1}$ are mainly assigned to the O-H stretching vibration and O-H bending vibration of the carboxylic groups. The $1633 \, cm^{-1}$ band can be attributed to the $C = O$ stretching vibration. The weak band at $1383 \, cm^{-1}$ is ascribed to the symmetric stretching vibration of COO^- the carboxyl group that validates that the MWCNTs were functionalized well.

Dex was loaded on SA1, and the FTIR spectrum of this sample is shown in Figure 3(b) to indicate specific chemical bands at different wavenumbers. Detected peaks around $3735 \, cm^{-1}$ and $1664 \, cm^{-1}$ were concerned with –NH stretching and bending vibration modes, respectively, which are due to the CTAB molecules. The broad peaks around $3420 \, cm^{-1}$ and $1491 \, cm^{-1}$ are attributed to stretching and bending vibration of OH groups, respectively, that are due to drug loading on the surface of the adsorbent. The symmetric and unsymmetrical stretching vibration of the C-H groups were observed at $2849 \, cm^{-1}$ and $2918 \, cm^{-1}$, respectively. The adsorption band at $1110 \, cm^{-1}$ was assigned to the P-O stretching vibration due to sodium phosphate groups in the dex structure. The peak around $1594 \, cm^{-1}$ is due to the C-N stretching vibration. Furthermore, the FTIR spectrum of O-MWCNT/PEG4000/dex is displayed in Figure 3(c). The adsorption peak at $1383 \, cm^{-1}$ is concerned with C-O groups of PEG and symmetric stretching vibration of COO^- the carboxyl group. The symmetric and asymmetric stretching vibrations of C-H groups were observed around $2852 \, cm^{-1}$ and $2912 \, cm^{-1}$ of dex and PEG, respectively. The weak peak at $1629 \, cm^{-1}$ describes the stretching vibration of the $C = O$ group. In addition, the stretching vibration of the P-O group can be observed at $1083 \, cm^{-1}$. In addition, the stretching vibration bands of $C = O$ and P-O groups were detected at $1633 \, cm^{-1}$ and $1068 \, cm^{-1}$, respectively, which is shown in Figure 3(d). The FTIR spectrum of TiO$_2$-O-MWCNT/dex is presented in Figure 3(e), and the presence of different functional groups and metal oxides in the synthesized samples is revealed. The observed peaks around $1458 \, cm^{-1}$, $2919 \, cm^{-1}$, and $2850 \, cm^{-1}$ indicate the bending vibration, symmetric stretching vibration, and asymmetric stretching vibration of the C-H group of the adsorbed dex, respectively. The carboxylate group can be observed at $1383 \, cm^{-1}$ again. The IR band at $1036 \, cm^{-1}$ presented the stretching vibration of P-O of drug molecules. In addition, the very strong peaks in the range of $521 \, cm^{-1}$–$669 \, cm^{-1}$ are assigned to the Ti-O stretching vibration of the group.

The morphology and size of the synthesized catalysts were investigated using the SEM technique, which is shown in Figure 4. Figure 4(a) shows the SEM image of the O-MWCNT/CTAB/dex sample with an average diameter of 30 nm. This is higher than the purchased MWCNTs (15 nm) due to the CTAB coverage. Figure 4(b) shows the SEM images of O-MWCNT/PEG4000/dex. It can be seen that carbon nanotubes were adhered together, which may be due to the presence of PEG. The shape and size of the MWCNTs are uniform, and the average diameter of the nanotubes is in the range of 30–40 nm. Figure 4(c) shows the SEM image of Au-O-MWCNT nanocomposites before dex adsorption. The average size of Au colloidal nanoparticles is about 30 nm. In addition, the images show that the Au nanoparticles were immobilized on the surface of carbon nanotubes uniformly with an average diameter of 25 nm. The SEM image of SA7 is shown in Figure 4(d). TiO$_2$ was dispersed uniformly on the MWCNT surface, and the average size of TiO$_2$ is about 40 nm.

In addition, the XRD pattern of the O-MWCNT sample is depicted in Figure 5(a). The noise of the intensity signals is due to the amorphous behavior and the low degree of crystallinity of the O-MWCNT nanocarrier. The fairly broad peaks observed at the angles (2θ) 25.6°, 43.7°, and 53.4° match with those of crystalline planes 002, 100, and 004, respectively, which corresponds to JCPDS card No.
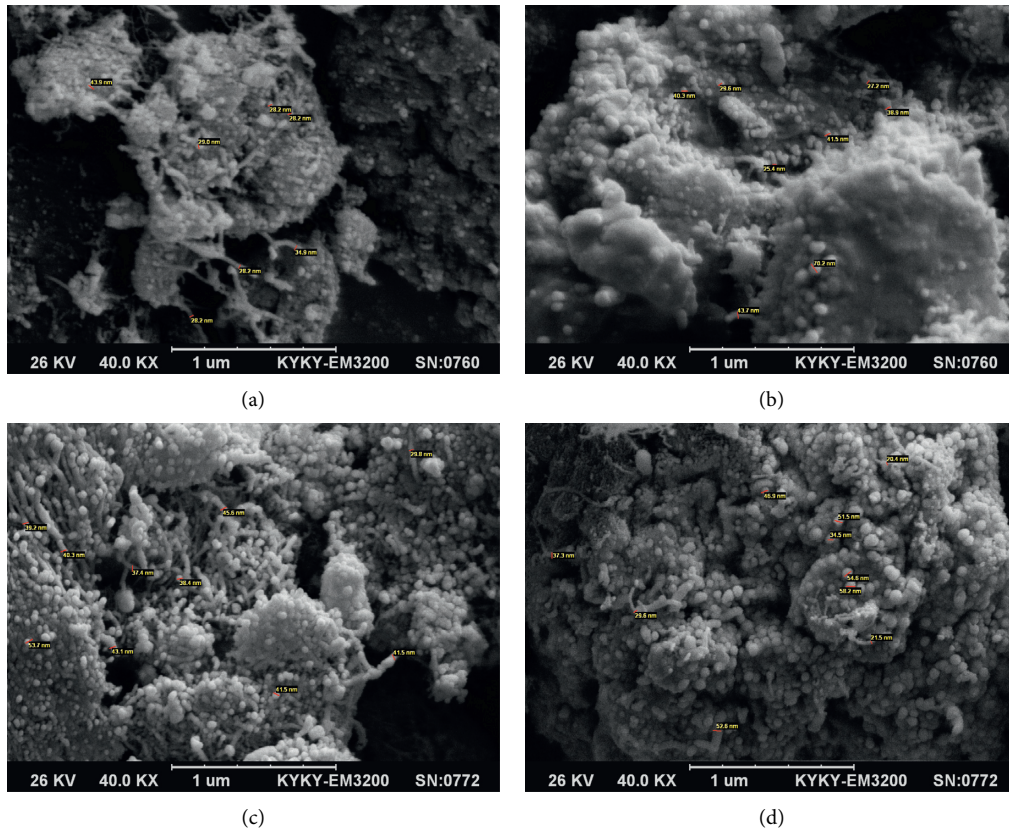
FIGURE 4: SEM images of prepared nanocarriers. (a) O-MWCNT/CTAB/dex, (b) O-MWCNT/PEG4000/dex, (c) Au-O-MWCNT: SA6, and (d) TiO$_2$-O-MWCNT: SA7.
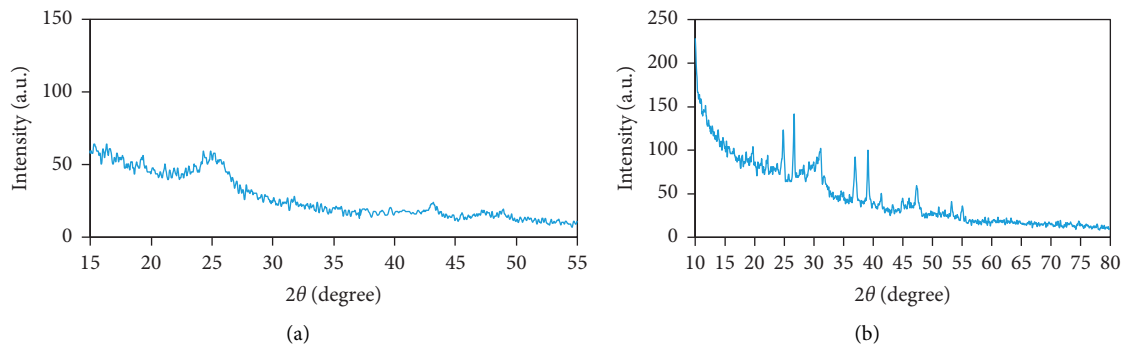

FIGURE 5: XRD patterns of samples. (a) O-MWCNTs (Cu anode with $\lambda = 1.54$ Å, 40 kV, 40 mA) and (b) O-MWCNT/PEG4000/dex (Co anode with $\lambda = 1.78$ Å, 40 kV, 40 mA).

41–1487. Furthermore, the addition of small amounts of PEG and dex to O-MWCNTs influenced the initial peaks to produce the sharp peaks. Furthermore, the XRD spectrum of O-MWCNT/PEG4000/dex can be observed in Figure 5(b). All main peaks of O-MWCNTs appeared at a similar position with higher intensity; moreover, some new peaks were detected over the O-MWCNT/PEG4000/dex sample. Overall, six diffraction peaks were observed (using cobalt anode with $\lambda = 1.78$) at angles (2θ), 19.8, 26.6, 37.3, 39.6, 48.6, and 53.1°, which correspond to 002, 060, 072, 452, 580, and 801 crystalline planes, respectively. The new

recorded peaks of the XRD pattern correspond to the JCPDS card No. 39–1691 of dexamethasone.

3.2. Optimum Operating Conditions for Adsorption Batch Studies

3.2.1. Optimum Adsorption Temperature. To elucidate the optimum temperature for the adsorption of dex, the removal percent of dex versus different temperatures for SA1 is depicted in Figure 6, and the data are reported in Table 3. It is necessary
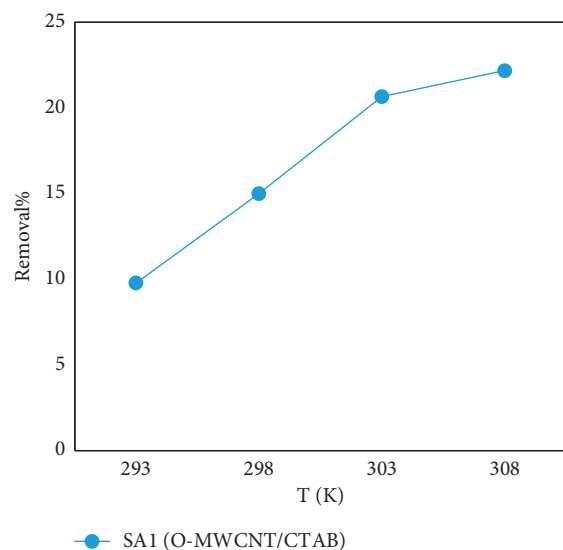
FIGURE 6: The effect of temperature on the dex removal percent for SA1 (dex initial concentration: $C_0 = 6.2e - 5$, adsorbent weight = 0.006 (g), adsorption time = 30 min, pH = 7.3).

TABLE 3: The adsorption capacity and removal percent of dex adsorbed onto SA1 at dex initial concentration: $C_0 = 6.2e - 5$, adsorbent weight = 0.006 g, adsorption time = 30 min, pH = 7.3.

T/K	q_e/mg · g^{-1} × 10^4	%Removal
293	2.02	9.79
298	3.1	15
303	4.27	20.67
308	4.58	22.19

to mention that the surfactant and dex were added to the O-MWCNTs, respectively; and only post-treatment processes, such as purification and drying steps, were carried out for the characterization of SA1 and was omitted in dex loading.

As it is expected, the amount of the removal percent of dex was highly enhanced with temperature increment that maximum removal percent was gained at 308 K. Since increasing the adsorption temperature can destruct the drug, 303 K is proposed as the optimum temperature for dex loading onto SA1. Similar experiments were conducted on other nanoadsorbents that showed the same results for temperature. This may be due to the fact that the O-MWCNTs were applied as the main part of all synthesized nanoadsorbents. In other words, the temperature adjusted for O-MWCNTs (as the support of nanocarriers) can be generalized to all samples.

3.2.2. Optimum Contact Time. The effect of adsorption time was analyzed at different time intervals for all synthesized adsorbents (Table 3). The adsorption capacity at different times was monitored and compared in order to understand the equilibrium contact time for each adsorbent. All experiments were conducted under similar conditions. Dex adsorption amounts should be calculated according to equation (4) (Table 4).

The amounts of q_t are depicted versus time in Figure 7 for all samples to achieve the optimum adsorption time. It can be seen that the amount of dex adsorbed onto SA1 was increased even after a short time with a steep slope. The maximum adsorption capacity on SA1 was achieved in 80 min, that is, about 57.59% and remains constant after this time. Since there was no considerable increase in drug loading after 80 min, the optimum adsorption time of 80 min was considered for SA1. This is due to the occupation of active sites by drug molecules, whereby the system reaches the equilibrium state. In the next step, the effects of surfactant on the adsorption potency of O-MWCNTs were examined. Therefore, SA2 was applied to further studies, and the concentration of remained dex was measured in the range 5–125 min. Interestingly, the amount of adsorbed dex for the SA2 sample is markedly greater than SA1 that depends on the surfactant. In other words, PEG 4000 can drastically enhance the adsorption rate of dex due to the active sites of the surface area. As a result, all samples that possess PEG 4000 were applied to drug loading in this study. The results show that the adsorption curve of SA2 reached a plateau at 85 min (adsorption capacity = 305.14 mg g^{-1}), and the removal percent is above 76%.

Metals have been routinely introduced to the structure of different adsorbents, which improves the adsorption performance. Herein, Au and TiO$_2$ were used in adsorbent synthesis. First, different amounts of Au were immobilized on the surface of the O-MWCNTs to determine the optimum value. Plots of adsorption capacity vs. contact time for different adsorbents are depicted in Figure 7. As it was expected, the adsorption amounts were increased for all mentioned samples, and then became constant. It can be observed that the ascending trend of adsorption performance was more or less similar for all the Au adsorbents in the order: SA3 > SA4 > SA5 > SA6. Quite remarkable is the increase in Au-concentration results in the lowering of the adsorption capacity at the onset of an adsorption period (45 min) relative to SA2. Although the experimental results show that the adsorption capacity of dex for Au-based samples surpassed that of the SA2 sample gradually. Thus, the ultimate adsorption uptakes for all Au supported adsorbents are higher than SA2. Considering the experimental data, it can be observed that the optimum adsorption time is 115 min, and the Au increment did not show a significant and enormous effect on the equilibrium state.

Furthermore, two designated samples of TiO$_2$ were examined for dex loading in order to check their adsorption potency. The remaining concentration of dex in the solution was measured using UV spectra (at 238 nm) continuously for the entire adsorption duration. It can be seen in Figure 7 that the adsorption capacity and removal percent of the drug were increased with a steep slope, and q_e became constant after 85 min. It can be observed that increasing the TiO$_2$ to O-MWCNT ratio from (1 : 4) to (1 : 2) rises the adsorption capacity from 290 mg · g^{-1} to 320 mg · g^{-1}. In addition, the removal percent increases about 7%, which is considerable in industrial applications. The comparison of the results shows that the most efficient synthesized drug nanocarrier is TiO$_2$-O-MWCNTs:1/2(SA7) with a maximum removal percent of 80%.

TABLE 4: Experimental data for adsorption capacity at a given time for different adsorbents: SA1, SA2, SA3, SA4, SA5, SA6, SA7, and SA8 at 303 K, dex initial concentration: $C_0 = 6.2e - 5$, adsorbent weight = 0.006 g, pH = 7.3.

Time	$q_t/\text{mg} \cdot \text{g}^{-1}$							
	SA1	SA2	SA3	SA4	SA5	SA6	SA7	SA8
5	4.3	273.58	227.02	235	243.3	256.06	307.05	259.14
15	23.83	274.79	234.04	253.64	260.59	266.27	309.95	261.02
25	25.55	281.24	245.82	259.6	269.43	272.97	312.16	268.87
35	34.14	284.3	265.57	270.23	273.1	273.42	312.95	279.13
45	—	292.82	266.5	278.24	280.69	289.66	315.89	286.12
50	41.32	—	—	—	—	—	—	—
55	—	292.88	284.43	278.88	296.39	294.7	316.02	286.44
65	56.31	299.17	288.64	291.45	296.04	301.4	316.62	288.51
75	—	303.44	291.16	307.4	305.46	304.3	318.63	289.69
80	57.59	—	—	—	—	—	—	—
85	—	305.14	301.21	308.87	306.83	305.36	320.13	295.83
95	58.23	306.22	309.25	309.51	310.59	309.48	320.55	296.27
105	—	306.35	313.15	313.46	313.68	313.85	320.74	296.62
110	58.55	—	—	—	—	—	—	—
115	—	306.41	313.21	313.85	315.12	315.28	320.84	297.19
125	—	306.44	313.3	314.93	315.57	316.21	320.9	297.41
135	—	—	313.34	314.29	315.98	317.04	—	—

3.2.3. Kinetic Models.

Different kinetic models were used to demonstrate the adsorption activity of functionalized MWCNTs loaded with metal oxides. The kinetic plots were investigated. The results (Figure 7) show a high adsorption efficiency for all synthesized samples. It was found that metal immobilization on the surface of adsorbents improved seriously the adsorption efficiency of dex. It was speculated that this effect emerges due to offering new active sites with high affinity compared to O-MWCNTs. The kinetic data were fitted with pseudo-first order, pseudo-second order, Elovich, and intraparticle models in Figures 8–10 and 11, respectively, and the models were compared together. All parameters and regression coefficients of aforementioned kinetic models are presented in Table 5. It was found that the pseudo-first order model shows a high degree of fitness for SA5, SA6, and SA7 with correlation coefficients all above 0.93. The correlation coefficients for other samples were all lower than 0.9, which demonstrated that the pseudo-first order kinetic model is not consistent with the experimental data. Figure 8 shows, in most cases, that the pseudo-first order kinetic model did not fit well over the whole range of contact time.

The $q_{e-\text{cal}}$ and the first order kinetic constant k_1 were calculated from the slope and intercept of the pseudo-first order model. Since the adsorption of dex upon other solid adsorbents did not follow the pseudo-first model, the experimental data were examined with the pseudo-second order model to understand the kinetic dynamics of adsorption. This model describes the chemisorption on adsorbents. In the next attempt, the experimental data were analyzed with the pseudo-second order kinetic model, and the results were compared together. The plot of t/q_t versus t gives a linear relationship (Figure 9) in which $q_{e-\text{cal}}$ and k_2 can be determined from the slope and intercept of the linear kinetic model.

The results show that the correlation coefficients of the pseudo-second order kinetic model for all samples (except SA1) were more than 0.99, indicating that the adsorption of dex on O-MWCNT-based adsorbents (except SA1) was followed by chemical mechanism. Since pseudo-first and second order kinetic models did not show good agreement with the experimental data of SA1, the absorption properties of dex on SA1 were investigated using the Elovich kinetic model in Figure 10.

It was found that the correlation coefficient of the Elovich model for SA1 was above 0.92, indicating a good agreement between theoretical predictions with experimental data. In other words, the correlation coefficient of the Elovich model was higher than that of the pseudo-first and second order models. Therefore, the Elovich model described the kinetics of dex adsorption on the O-MWCNTs accurately.

To identify the diffusion mechanism, experimental data were analyzed by using the intraparticle diffusion model proposed by Weber and Morris. The rate-controlling step in diffusion can be determined using the intraparticle model. The proposed adsorption mechanism occurs in two stages. In the first stage, dex molecules were diffused through a boundary layer surrounding the surface of adsorbents, and in the next stage, dex molecules diffuse toward the tortuous pores with an interaction between adsorbate species and adsorbent (intraparticle diffusion). For the regression of Weber and Morris diffusion model, a plot of q_t versus $t^{1/2}$ was depicted, and the diffusion rate constants and C values were obtained from the slope and intercept of distinct linear portions of the diffusion plot. The parameters of the Weber–Morris model are reported in Table 5 in detail. The intraparticle multistage linear fit for the adsorption of dex upon SA1 adsorbent is depicted in Figure 11(a), and the coefficients calculated from it are shown in Table 5. It can be seen that the plot consists of two distinct linear parts, indicating a two-stage diffusion mechanism in adsorption. The high values of regression coefficients r_1^2 and r_2^2 indicate that the intraparticle mechanism well illustrates the adsorption of dex in the case O-MWCNT/CTAB.
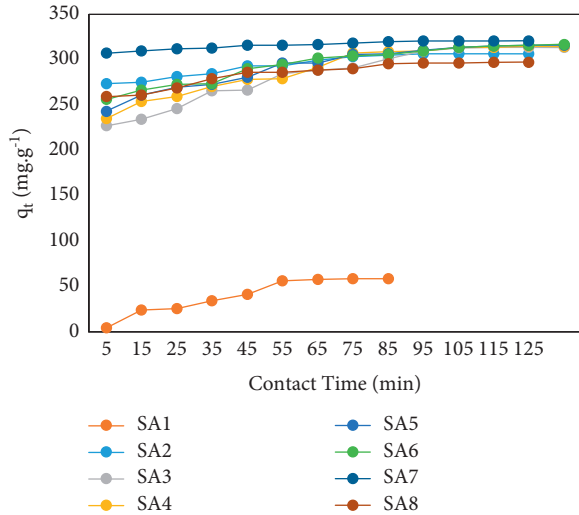
FIGURE 7: The effect of contact time on dex adsorption on different adsorbents (dex initial concentration: $C_0 = 2.3237e - 5$, $T = 303$ K, pH = 7.3, adsorbent weight = 0.006 (g)).
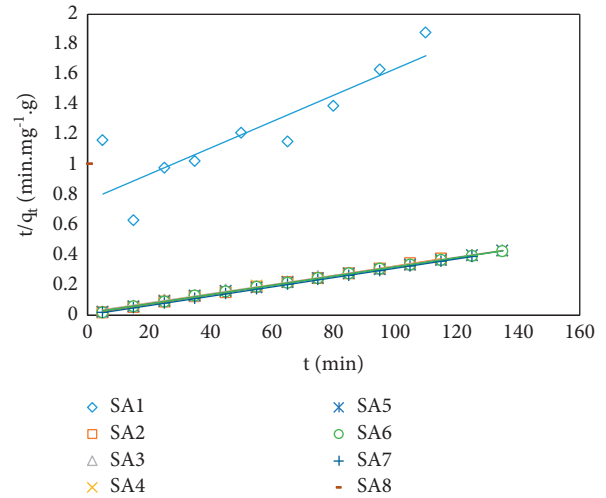

FIGURE 9: The plot of the pseudo-second order model of dex adsorption onto different adsorbents (dex initial concentration: $C_0 = 2.3237e - 5$, $T = 303$ K, pH = 7.3, adsorbent weight = 0.006 (g)).
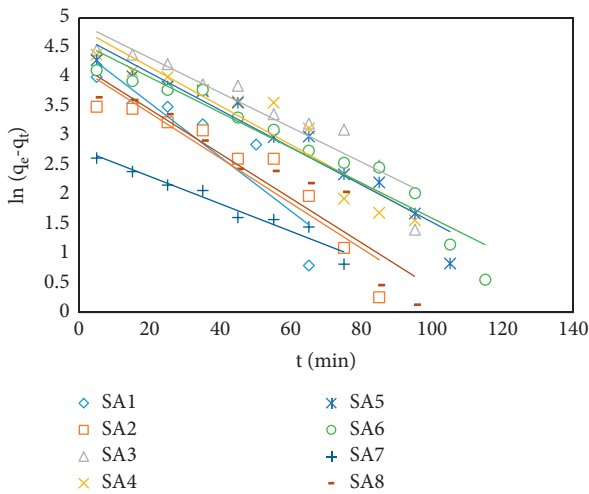

FIGURE 8: The plot of pseudo-first order model of dex adsorption onto different adsorbents (dex initial concentration: $C_0 = 2.3237e - 5$, $T = 303$K, pH = 7.3, adsorbent weight = 0.006 (g)).
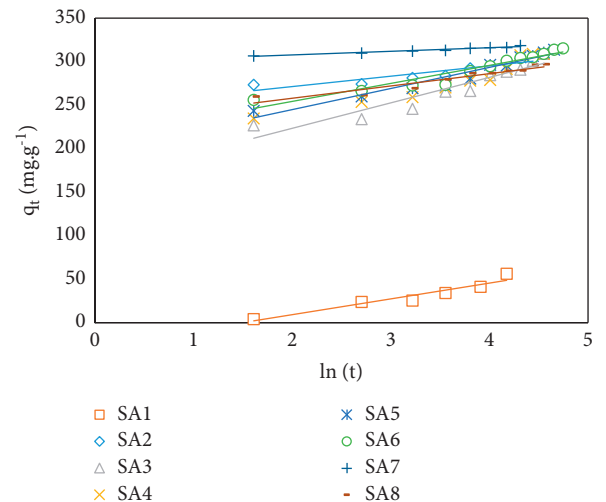

FIGURE 10: The plot of the Elovich model of dex adsorption onto different adsorbents (dex initial concentration: $C_0 = 2.3237e - 5$, $T = 303$ K, pH = 7.3, adsorbent weight = 0.006 (g)).

Conspicuously, the first stage line with the intercept -12.613 mg g^{-1} does not pass through the origin (shows low deviation), which suggests that both boundary layer diffusion and intraparticle diffusion contributed to the overall adsorption process. Although, the first portion (stage I) was only attributed to the dex diffusion through the bulk to the exterior surface of the adsorbents. The comparison between the two stages shows that the linear slope of the first portion k_{i1} is significantly larger than the slope of the second portion k_{i2}, which refers to the faster adsorption rate of bulk diffusion in comparison to the intraparticle diffusion. In other words, the intraparticle diffusion is the rate controlling step in the adsorption process by SA1.

The Weber and Morris diffusion model for dex diffusion through SA2 was investigated, and the plot is depicted in Figure 11(b). The results show significant deviation from the

origin, which was represented by the intercept of the first stage linear plot. This can be accounted by the fact that both film diffusion and intraparticle diffusion participated in the adsorption process. First, dex molecules quickly diffused through the film with a steep slope. The second portion (stage II) followed by the intraparticle diffusion of dex molecules within the CNTs. It was speculated that the second part is the rate-limiting step due to the gradual diffusion of species. Figure 11(c) shows the adsorption of dex on the Au-O-MWCNT samples (SA3, SA4, SA5, and SA6). According to the experimental results, the adsorption process can be divided into two phases for these Au-based adsorbents. It was found that both boundary layer diffusion and intraparticle diffusion control the diffusion mechanism of all four mentioned cases.
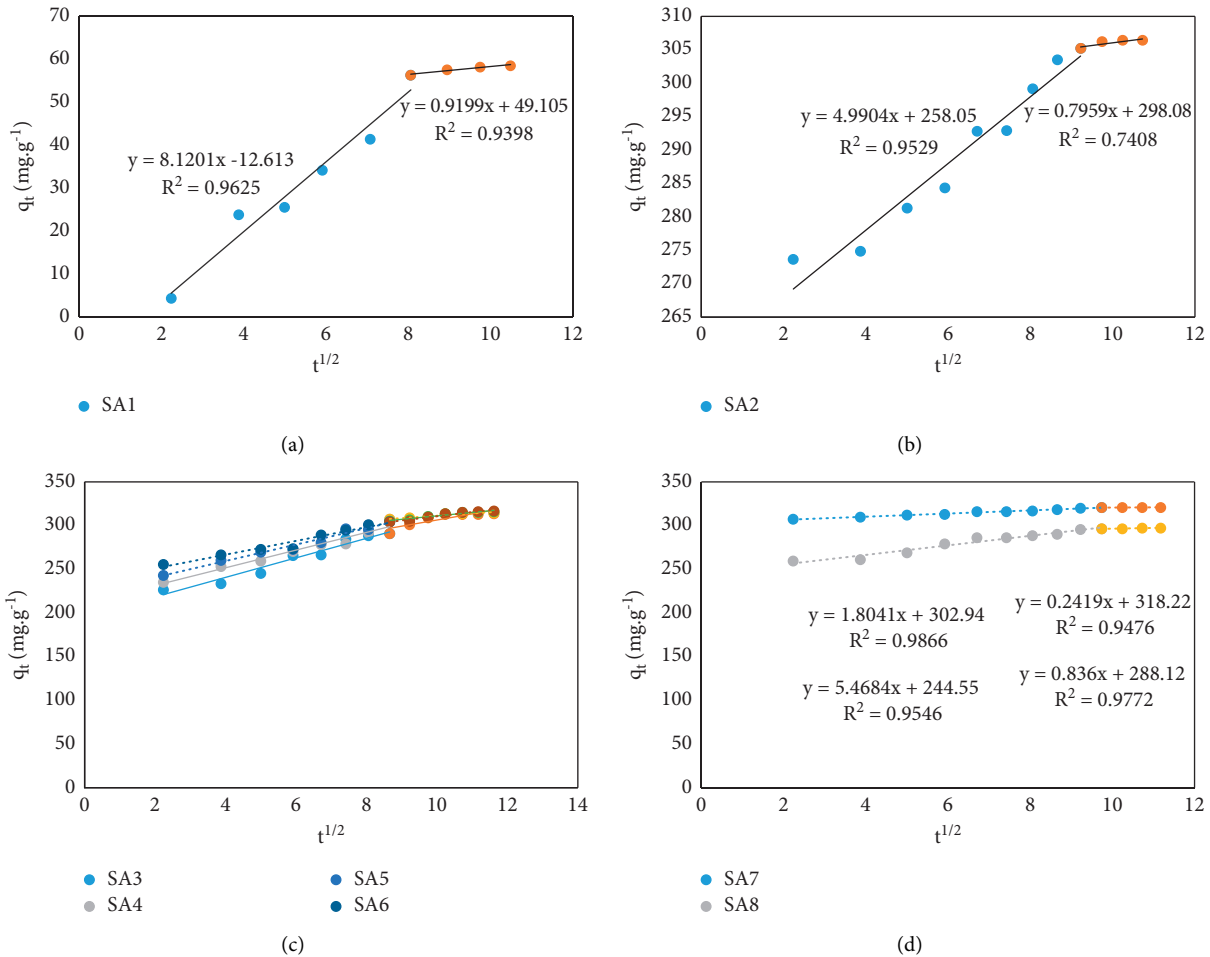
FIGURE 11: The plot of the intraparticle model of dex adsorption onto different adsorbents (dex initial concentration: $C_0 = 2.3237e - 5$, $T = 303$ K, pH = 7.3, adsorbent weight = 0.006 (g)). (a) SA1, (b) SA2, (c) SA3, SA4, SA5, SA6, and (d) SA7, SA8.

The adsorption kinetic model of TiO$_2$-O-MWCNT samples are depicted in Figure 11(d). It was worthy to mention that the solute diffused through the film and the pores slowly relative to other adsorbents. Comparing the rate constants of stage I and stage II for the SA7 adsorbent, it can be concluded that both mechanisms (film diffusion and intraparticle diffusion) control the dex adsorption onto the TiO$_2$-based samples.

3.3. Isotherm Models.
To determine the best model to better understand the system behavior, different isotherms were applied and compared together. Molecular distribution between aqueous solution and the solid phase at the equilibrium state can be defined by adsorption isotherms. Moreover, equilibrium capacity and adsorbent efficiency can be calculated according to isotherm studies. The combination of different adsorption mechanisms due to the surface structure may result in more complexity in defining the system. Batch scale systems with different initial concentrations of dex on O-MWCNT-based samples (SA1, SA2, SA6, and SA7) were prepared to measure the equilibrium adsorption capacity. Adsorption experiments were carried

out in triplicate, and the average data for each case were reported in this investigation. The measured data of adsorption are listed in Table 6, comprehensively.

In the present work, Langmuir, Freundlich, Temkin, and Dubinin–Radushkevich isotherms were applied to the experimental data and studied in detail on different adsorbents. The regression coefficients r^2 and the parameters of adsorption isotherms for all isotherms are compared in Table 7 to select the best model for dexamethasone adsorption.

In the first attempt, Langmuir isotherm was developed based on a uniform and monolayer distribution on a homogeneous adsorbent, which is an ideal assumption. C_e/q_e versus C_e is plotted linearly in Figure 12 for all samples, and the constants of Langmuir were calculated.

The experimental data of C_e/q_e versus C_e of dex for SA1 at the equilibrium state were fitted to the Langmuir isotherm with a linear relationship with regression coefficient $r^2 = 0.958$. K_L and q_{max} for SA1 were derived from the slope and the intercept of the Langmuir linear isotherm 0.1655 and 0.9583. The results show that increasing the Au amount improves the adsorption capacity from 437.78 mg $\cdot$ g^{-1} (SA1) to 476.19 mg $\cdot$ g^{-1} (SA6) slightly. This indicates the stronger interaction between dex and

TABLE 5: Experimental data for kinetic study in different adsorbents: SA1, SA2, SA3, SA4, SA5, SA6, SA7, and SA8 at 303 K, dex initial concentration: $C_0 = 6.2e - 5$, adsorbent weight = 0.006 g, pH = 7.3.

Model	Parameters	Samples							
		SA1	SA2	SA3	SA4	SA5	SA6	SA7	SA8
Pseudo-first order	k_1/min^{-1}	0.0459	0.0383	0.0295	0.033	0.0317	0.0299	0.0233	0.0378
	r^2	0.8174	0.8795	0.8902	0.8984	0.9415	0.93	0.9509	0.8942
	$q_e/\text{mg} \cdot \text{g}^{-1}$	87.51	63.33	135.14	124.4	109.76	98.14	16.01	66.78
Pseudo-second order type (I)	$k_2/\text{g} \cdot \text{mg}^{-1} \cdot \text{min}^{-1}$	0.0001	0.0013	0.0004	0.00049	0.0006	0.00069	0.0038	0.0013
	r^2	0.7592	0.9995	0.9973	0.9979	0.9988	0.999	1	0.9997
	$q_e/\text{mg} \cdot \text{g}^{-1}$	113.63	312.5	333.33	333.33	322.58	322.58	322.58	322.58
	$\Delta q\%$								
Elovich	r^2	0.9244	0.8425	0.8923	0.8923	0.9409	0.9148	0.948	0.9054
	$\alpha/\text{mg} \cdot \text{g}^{-1} \cdot \text{min}^{-1}$	4.085	1.2e-10	8214	8214	79545	611232	7.7e31	1.61e8
	$\beta/\text{g} \cdot \text{mg}^{-1}$	0.055	0.08385	0.0341	0.0341	0.041	0.0483	0.24	0.0707
Intraparticle	k_{i1}/min^{-1}	8.1201	4.9904	11.171	10.118	9.388	7.8617	1.8041	5.4684
	$C_1/\text{mg} \cdot \text{g}^{-1}$	−12.613	258.05	196.05	211.26	221.94	235.3	302.95	244.55
	r_1^2 (stage I)	0.9625	0.9529	0.9604	0.9588	0.9757	0.9559	0.9866	0.9546
	k_{i2}/min^{-1}	0.9199	0.7959	7.0358	2.7161	3.9239	4.8008	0.24198	0.836
	$C_2/\text{mg} \cdot \text{g}^{-1}$	49.105	298.08	236.04	284.06	271.87	262.68	318.22	288.12
	r_2^2 (stage II)	0.9398	0.7408	0.7676	0.8922	0.9287	0.9417	0.9476	0.9772

TABLE 6: The measured data for dex adsorption onto different synthesized samples: SA1, SA2, SA6, and SA7 at 303 K, dex initial concentration: $C_0 = 6.2e - 5$, adsorbent weight = 0.006 g, pH = 7.3.

$C_0/\text{mol} \cdot \text{l}^{-1}$	$C_e/\text{mol} \cdot \text{l}^{-1}$	$q_e/\text{mg} \cdot \text{g}^{-1}$	C_e/q_e	$\ln C_e$	$\ln q_e$	ε^2
			SA1			
0.0000155	3.274767	157.507763	0.020791	1.186247	5.059474	4.506×10^5
0.0000194	4.557488	181.417069	0.025122	1.516772	5.200799	2.497×10^5
0.0000271	7.218655	226.044834	0.031935	1.976669	5.420733	1.068×10^5
0.000031	8.252490	258.250344	0.031955	2.110515	5.553929	8.302×10^4
			SA2			
0.0000155	3.877837	137.405	0.0282	1.355	4.922	3.34×10^5
0.0000194	5.419017	152.699439	0.035488	1.689914	5.028472	1.82×10^5
0.0000271	8.606674	179.777540	0.047874	2.152538	5.191720	7.667×10^4
0.000031	9.717089	209.430372	0.046398	2.273886	5.344391	6.088×10^4
			SA6			
0.0000155	3.36	154.64	0.0217	1.21	5.04	4.3×10^5
0.0000194	4.94	168.65	0.0293	1.6	5.13	2.15×10^5
0.0000271	6.99	233.38	0.03	1.95	5.45	1.13×10^4
0.000031	8.46	251.23	0.0337	2.14	5.53	7.92×10^4
			SA7			
0.0000155	3.72	142.57	0.0261	1.31	4.96	3.59×10^5
0.0000194	5.2	160.07	0.0325	1.65	5.08	1.96×10^5
0.0000271	8.26	191.39	0.0431	2.11	5.25	8.28×10^4
0.000031	9.45	218.43	0.0433	2.25	5.39	6.42×10^4

SA6 rather than that with SA1. In the cases of SA1 and SA7 adsorbents, the r^2 values of the Langmuir adsorption isotherm close to unity ($r^2 > 0.95$) demonstrate the good agreement between the experimental data and theoretical results. This indicates that, in these adsorbents composed of a homogeneous surface, all adsorption sites are energetically equivalent. Therefore, the physical binding of dex molecules with the active sites is monolayer adsorption. The adsorption rate constant K_L of SA1 was measured to be 0.165, which is lower than SA7 (0.2), which implies a lower adsorption rate. It can be seen that Langmuir shows a significant deviation from the straight line for SA2 and SA6 samples. This means that Langmuir cannot describe the

adsorption behavior in the absence of experimental data for these two cases. In addition, the separation factor R_L for all cases was $0 < R_L < 1$, demonstrating that the adsorption process was favorable under the examined condition.

Furthermore, Lnq_e values are plotted against LnC_e in Figure 13, and K_F $1/n$ were determined from the slope and the intercept of the linear Freundlich relationship for all adsorbents.

It is clear that the efficiency of SA1 for drug adsorption is higher than the other samples due to the highest value of K_F. K_F shows the Freundlich constant that was calculated to be $84.29 \text{ mg} \cdot \text{g}^{-1}$ for the SA1 sample. The separation factor $1/n$ indicates that the surface uniformity was (0.5151,

TABLE 7: The constants of Langmuir, Freundlich, Temkin, and Dubinin–Radushkevich for adsorption of dex on different O-MWCNT-based samples: SA1, SA2, SA6, and SA7 at 303 K, dex initial concentration: $C_0 = 6.2e-5$, adsorbent weight = 0.006 g, pH = 7.3.

| Isotherm	Parameters	Sample			
		SA1	SA2	SA6	SA7
Langmuir	$q_{max}/\mathrm{mg} \cdot \mathrm{g}^{-1}$	437.78	303.03	476.19	322.58
	$K_L/\mathrm{L} \cdot \mathrm{mg}^{-1}$	0.165	0.2	0.128	0.2
	R_L	0.43091–0.2746	0.38449–0.23799	0.4939–0.3279	0.3845–0.2379
	r^2	0.9583	0.9397	0.8594	0.9635
Freundlich	$K_F/\mathrm{mg} \cdot \mathrm{g}^{-1} (\mathrm{L} \cdot \mathrm{mg})^{-1/n}$	84.293	75.88	74.71	79.97
	$1/n$	0.5151	0.4243	0.5645	0.4308
	r^2	0.983	0.9442	0.9372	0.967
Temkin	$B_T/\mathrm{J} \cdot \mathrm{mol}^{-1}$	103.97	71.4	111.28	76.006
	$A_T/\mathrm{L} \cdot \mathrm{mg}^{-1}$	1.3256	1.67	1.096	1.67
	r^2	0.9635	0.9145	0.922	0.95
Dubinin–Radushkevich	$q_D/\mathrm{mg} \cdot \mathrm{g}^{-1}$	266.85	209.41	245.16	221.47
	$K_{DR} \times 10^6/(\mathrm{mol} \cdot \mathrm{J}^{-1})^2$	1.25	1.36	1.17	1.31
	$E/\mathrm{kJ} \cdot \mathrm{mol}^{-1}$	0.632	0.606	0.653	0.617
	r^2	0.9123	0.8555	0.8117	0.8866
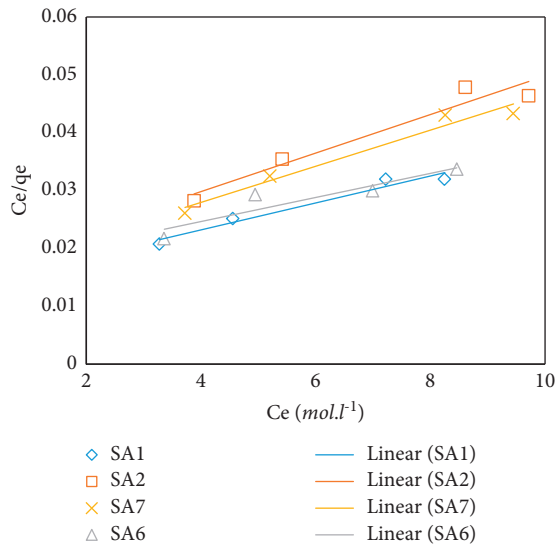
FIGURE 12: Langmuir isotherms for dex adsorption on O-MWCNT-based adsorbents, adsorbent weight = 0.006 (g), contact time = 65 min, $T = 30℃$, and pH = 7.3.
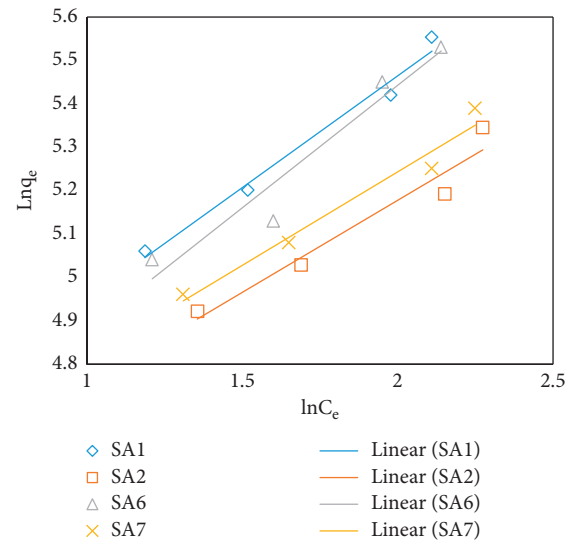

FIGURE 13: Freundlich isotherms for dex adsorption on O-MWCNT-based adsorbents, adsorbent weight = 0.006 (g), contact time = 65 min, $T = 30℃$, and pH = 7.3.

0.4243, 0.5645, and 0.4308) for SA1, S2, SA6, and SA7, respectively. Since $0 < 1/n < 1$, the adsorption process belongs to a favorable range. This means that multilayer adsorption took place at the heterogeneous sites of the adsorbent surface with nonuniform adsorption heat. This adsorption is reversible. Since, n is greater than unity, the system in this study underwent physisorption mechanism and chemical adsorption did not happen. Furthermore, all equilibrium data obtained for samples were fitted to Temkin and Dubinin–Radushkevich isotherms and are reported in Table 7 in detail. Figure 14 illustrates the variation in the equilibrium capacity with LnC_e to determine Temkin constants.

The maximum heat of adsorption (B_T) and minimum equilibrium binding energy (A_T) for SA6 were obtained as $111.28\,\mathrm{J} \cdot \mathrm{mol}^{-1}$ and $1.096\,\mathrm{L} \cdot \mathrm{mg}^{-1}$, respectively, with regard to the Temkin isotherm. The highest value of

A_T ($1.67\,\mathrm{L} \cdot \mathrm{mg}^{-1}$) was obtained for SA2, and SA7 shows the binding strength between dex molecule and the active site of the carrier. Furthermore, the Dubinin–Rudeshkevich model was applied to experimental data that can be seen in Figure 15.

The theoretical saturation capacity q_D for the Dubinin–Radushkevich isotherm increased as $SA1 < SA6 < SA7 < SA2$, which indicates that adsorption is facilitated by adding the metal oxides and using PEG as a surfactant. The adsorption energy is $E < 8\,\mathrm{kJ} \cdot \mathrm{mol}^{-1}$, illustrating that the physical adsorption of dex occurred on all adsorbents.

Comparing the results shows that the Freundlich isotherm has the lowest deviation from the experimental data (highest value of r^2) and is the most appropriate model for predicting the results for all cases. On the other hand, the Freundlich isotherm shows the best fitting with experimental data for various nanoadsorbents. This confirms the
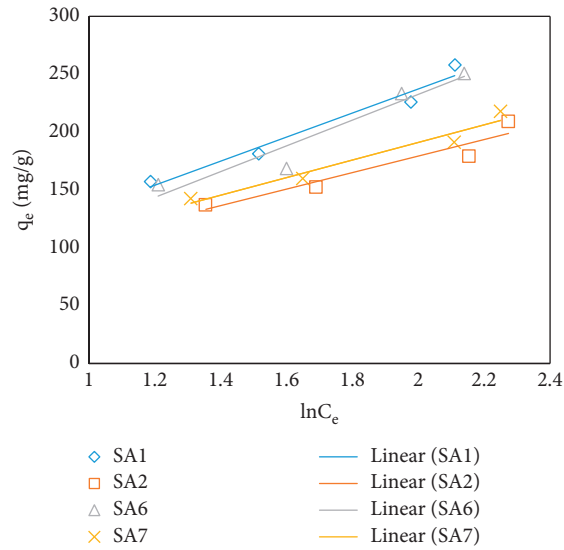
FIGURE 14: Temkin isotherms for dex adsorption on O-MWCNT-based adsorbents, adsorbent weight = 0.006 (g), contact time = 65 min, $T = 30°C$, and pH = 7.3.
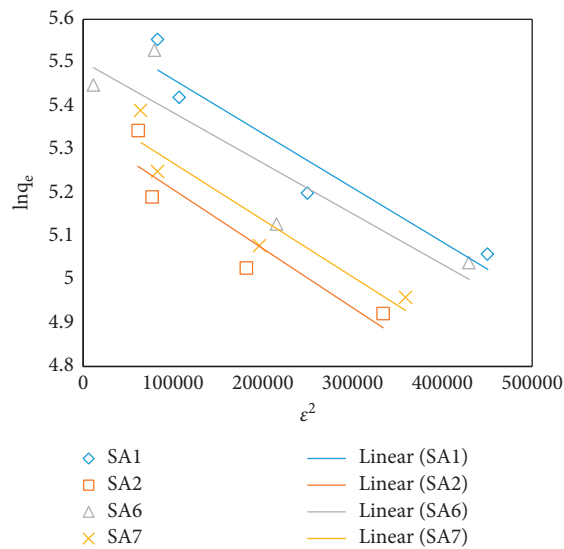

FIGURE 15: Dubinin–Radushkevich isotherms for dex adsorption on O-MWCNT-based adsorbents, adsorbent weight = 0.006 (g), contact time = 65 min, $T = 30°C$, and pH = 7.3.

TABLE 8: Recent studies about dex DDSs.

Nanocarrier	DEX loading method and results	Kinetic models	Ref
Poly(3,4-ethylenedioxythiophene) (PEDOT)	Dex was loaded on PEDOT polymer, fixed on the electrode probe, and release studies were carried out using cyclic voltammetry signals	—	[69]
Double-crosslinked hyaluronic acid hydrogel poly(L-lactide-co-glycolide) (PLGA)	Double-crosslinked hyaluronic acid hydrogels containing dexamethasone and PLGA/dexamethasone sodium phosphate (PLGADEX) nanoparticles were prepared. For all ratios of XHA/DEX, drug released nearly 90% after 3 days.	—	[2]
PLGA-PEG-PLGA hydrogel	The triblock copolymer PLGA-PEG-PLGA was applied for the dexamethasone carrier. The in vitro release was examined for various copolymer structures and drug concentrations.	Zero order $0.83 \leq R^2 \leq 0.916$ Higuchi $0.961 \leq R^2 \leq 0.987$	[70]
Multiwall carbon nanotubes (MWCNTs)	CNTs were pretreated with acid sonication, and the open ends of the drug-filled CNTs are sealed with polypyrrole (PPy) films.	—	[71]

TABLE 8: Continued.

Nanocarrier	DEX loading method and results	Kinetic models	Ref
Vertically aligned multiwall carbon nanotubes (VA-MWCNTs)	Dex-MWCNTs and dex-PEG-MWCNTs were prepared by using the precipitation method. Release study was conducted in 12 h. Dexamethasone release curve was obtained at different pH values	—	[72]

multilayer adsorption of dex molecules onto the surface of adsorbents. Each molecule of the drug has two Na^+ that can bond to COOH groups to form NaCOOH. This forms the first layer of adsorbates that can bind with other adsorbed layers, and a multilayer adsorption occurs. Regarding the highest value of r^2 obtained from the Freundlich model, it was suggested that this model is the best fit to the experimental data among the tested models. This implies that adsorption of dex on adsorbents takes place at the heterogeneous sites on the surface.

In recent years, the anticancer drug paclitaxel has been adsorbed onto Sylopute and Diaion HP-20. The isotherm models were analyzed based on experimental data [58, 64]. CNTs were primarily applied in cancer treatment. It is worthy to mention that a few studies have been devoted to MWCNTs in dex-targeted delivery. Among the relevant studies, a limited number have demonstrated the uptake analysis, including kinetic studies and isotherm models. Some of the studies conducted in this regard in recent years are reported in Table 8.

4. Conclusion

The long time use of dexamethasone shows some therapy failure. To overcome the side effects and drug inefficiency, CNTs were used as a drug carrier. In recent years, an increasing number of studies have been published analyzing the MWCNT role in developing the drug delivery systems due to their extraordinary properties. This research is devoted to the fabrication and analysis of the novel nanocomposites based on O-MWCNTs for dex-targeted delivery. In order to further take advantage, MWCNTs can be combined with Au and TiO_2 to form hybrid composites, including Au-O-MWCNTs and TiO_2-O-MWCNTs. The functionalization of MWCNTs by COOH as a hydrophilic group can improve the dex adsorption and reduce its cytotoxicity. Moreover, the organic surfactants (CTAB and PEG) were used for drug encapsulation or conjugation.

According to the experimental results, 303 K was defined as the optimum adsorption temperature for dex loading. Furthermore, the kinetic data were fitted with pseudo-first order, pseudo-second order, Elovich, and intraparticle models. Regarding the kinetic studies, within the first 85 min, good linearity with a steeper slope can be observed; however, after 85 min, another linearity with a smoother slope was observed (optimum adsorption time is 85 min).

Experimental results show that the pseudo-second order model is an appropriate model for interpreting the adsorption process on SA2, SA3, SA4, SA5, SA6, SA7, and SA8. However, the adsorption of dex onto SA1 did not correspond with the pseudo-second order model. The diffusion mechanism was investigated via Weber and Morris intraparticle diffusion model. The r^2 of the first portion for all cases was higher than 0.95, indicating that the adsorption of dex followed the intraparticle diffusion model. However, the straight lines did not pass through the origin, which shows that the intraparticle step is the rate limiting step, and bulk diffusion may contributed to the diffusion control. The k_{i1} is greater than k_{i2} for all samples, which is assigned to the importance of intraparticle diffusion (stage II). Similar phenomena were observed for all adsorbents, which suggests that both film diffusion and intraparticle diffusion contributed to the adsorption process.

The adsorption equilibrium data were applied to the Langmuir, Freundlich, Temkin, and Dubinin–Radushkevich isotherms. The maximum adsorption capacity for SA1 was measured to be $437.78 \, mg \cdot g^{-1}$ and is larger than q_{max} of SA7. This means that SA1 is a more appropriate nanocarrier for dex loading. The adsorption capacity was improved from $437.78 \, mg \cdot g^{-1}$ (SA1) to $476.19 \, mg \cdot g^{-1}$ (SA6) by increasing Au. According to the experimental data, the favorability of isotherms for SA1 and SA6 decreased in the order: Freundlich > Temkin > Langmuir > Dubinin–Radushkevich. However, for SA2 and SA7 adsorbents, Langmuir can predict the results more accurately than Temkin and favorability decreased in the order: Freundlich > Langmuir > Temkin > Dubinin–Radushkevich. For Temkin and Dubinin–Radushkevich models, the best fitting and highest r^2 values were obtained for SA1. The maximum heat of adsorption (B_T) and minimum equilibrium binding energy (A_T) for SA6 were obtained as $111.28 \, J \cdot mol^{-1}$ and $1.096 \, L \cdot mg^{-1}$ with regard to the Temkin isotherm.

Data Availability

The data are available on request.

Conflicts of Interest

The authors declare that they have no conflicts of interest.

Acknowledgments

References

[1] S. Tao Li, N. Nan Chen, Y. Biao Qiao, W. Li Zhu, J. Wei Ruan, and X. Zhong Zhou, "SC79 rescues osteoblasts from dexamethasone though activating Akt-Nrf2 signaling," *Biochemical and Biophysical Research Communications*, vol. 479, no. 1, pp. 54–60, 2016.

[2] Z. Mousavi Nejad, B. Torabinejad, S. Mohammad Davachi et al., "Synthesis, physicochemical, rheological and in-vitro characterization of double-crosslinked hyaluronic acid hydrogels containing dexamethasone and PLGA/dexamethasone nanoparticles as hybrid systems for specific medical applications," *International Journal of Biological Macromolecules*, vol. 126, pp. 193–208, 2019.

[3] X. Liang, B. Li, Q. Huang, D. Liu, and H. Ma, "Klotho prevents DEX-induced apoptosis in MC3T3-E1 osteoblasts through the NF-κB signaling pathway," *Biochemical and Biophysical Research Communications*, vol. 507, no. 1–4, pp. 355–361, 2018.

[4] C. Bucolo, L. Gozzo, L. Longo, S. Mansueto, D. C. Vitale, and F. Drago, "Long-term efficacy and safety profile of multiple injections of intravitreal dexamethasone implant to manage diabetic macular edema: a systematic review of real-world studies," *Journal of Pharmacological Science*, vol. 138, no. 4, pp. 219–232, 2018.

[5] V. Karthika, P. Kaleeswarran, K. Gopinath et al., "Biocompatible properties of nano-drug carriers using TiO2-Au embedded on multiwall carbon nanotubes for targeted drug delivery," *Mater Science and Engineering C*, vol. 90, pp. 589–601, 2018.

[6] T. T. Wang, F. Chai, C. G. Wang et al., "Fluorescent hollow/rattle-type mesoporous Au@SiO2nanocapsules for drug delivery and fluorescence imaging of cancer cells," *Journal of Colloid Interface Science*, vol. 358, no. 1, pp. 109–115, 2011.

[7] S. Kumari and R. P. Singh, "Glycolic acid functionalized chitosan-Au-Fe3O4hybrid nanoparticle based nanohybrid scaffold for drug delivery," *International Journal of Biological Macromolecules*, vol. 54, no. 1, pp. 244–249, 2013.

[8] T. Chen, T. Zhao, D. Wei, Y. Wei, Y. Li, and H. Zhang, "Core-shell nanocarriers with ZnO quantum dots-conjugated Au nanoparticle for tumor-targeted drug delivery," *Carbohydrate Polymers*, vol. 92, no. 2, pp. 1124–1132, 2013.

[9] M. A. A. Ragab, M. A. Korany, H. Z. Ibrahim, M. A. Abdel-Kawi, and A. E. A. A. A. Sayed, "Adsorption behavior of some metal ions on nanoparticles used in pharmaceutical matrices: application to laboratory made drug formulation," *Bulletin of Faculty Pharmacy, Cairo University*, vol. 55, no. 1, pp. 155–162, 2017.

[10] M. Gomar and S. Yeganegi, "Adsorption of 5-fluorouracil, hydroxyurea and mercaptopurine drugs on zeolitic imidazolate frameworks (ZIF-7, ZIF-8 and ZIF-9)," *Microporous Mesoporous Materials*, vol. 252, pp. 167–172, 2017.

[11] D. Lombardo, M. A. Kiselev, and M. T. Caccamo, "Smart nanoparticles for drug delivery application: development of versatile nanocarrier platforms in biotechnology and nanomedicine," *Journal of Nanomaterials*, vol. 2019, Article ID 3702518, 26 pages, 2019.

[12] S. Ghosh, R. Lalani, V. Patel et al., "Combinatorial nanocarriers against drug resistance in hematological cancers: opportunities and emerging strategies," *Journal of Controlled Release*, vol. 296, pp. 114–139, 2019.

[13] J. Y. Ljubimova, T. Sun, L. Mashouf et al., "Covalent nano delivery systems for selective imaging and treatment of brain tumors," *Advanced Drug Delivery Reviews*, vol. 113, pp. 177–200, 2017.

[14] D. Shcharbin, M. Bryszewska, S. Mignani, X. Shi, and J. P. Majoral, "Phosphorus dendrimers as powerful nanoplatforms for drug delivery, as fluorescent probes and for liposome interaction studies: a concise overview," *European Journal of Medicinal Chemistry*, vol. 208, Article ID 112788, 2020.

[15] D. George, P. U. Maheswari, and K. M. M. S. Begum, "Synergic formulation of onion peel quercetin loaded chitosan-cellulose hydrogel with green zinc oxide nanoparticles towards controlled release, biocompatibility, antimicrobial and anticancer activity," *International Journal of Biological Macromolecules*, vol. 132, pp. 784–794, 2019.

[16] A. Ahmad, N. M. Mubarak, K. Naseem et al., "Recent advancement and development of chitin and chitosan-based nanocomposite for drug delivery: critical approach to clinical research," *Arabian Journal of Chemistry*, vol. 13, no. 12, pp. 8935–8964, 2020.

[17] B. Dutta, N. G. Shetake, B. K. Barick, B. N. Pandey, K. I. Priyadarsini, and P. A. Hassan, "pH sensitive surfactant-stabilized Fe3O4 magnetic nanocarriers for dual drug delivery," *Colloids Surfaces B Biointerfaces*, vol. 162, pp. 163–171, 2018.

[18] H. Hashemzadeh and H. Raissi, "Understanding loading, diffusion and releasing of doxorubicin and paclitaxel dual delivery in graphene and graphene oxide carriers as highly efficient drug delivery systems," *Applied Surface Science*, vol. 500, Article ID 144220, 2020.

[19] E. Heister, V. Neves, C. Lamprecht, S. R. P. Silva, H. M. Coley, and J. McFadden, "Drug loading, dispersion stability, and therapeutic efficacy in targeted drug delivery with carbon nanotubes," *Carbon*, vol. 50, no. 2, pp. 622–632, 2012.

[20] Y. Wang and C. Wang, "Self-assembly of graphene sheets actuated by surface topological defects: toward the fabrication of novel nanostructures and drug delivery devices," *Applied Surface Science*, vol. 505, Article ID 144008, 2020.

[21] R. Jha, A. Singh, P. K. Sharma, and N. K. Fuloria, "Smart carbon nanotubes for drug delivery system: a comprehensive study," *Journal of Drug Delivery Science and Technology*, vol. 58, 2020.

[22] M. R. Awual, "A novel facial composite adsorbent for enhanced copper(II) detection and removal from wastewater," *Chemical Engineering Journals*, vol. 266, pp. 368–375, 2015.

[23] R. Awual, "An efficient composite material for selective lead(II) monitoring and removal from wastewater," *Journal of Environmental Chemical Engineering*, vol. 7, no. 3, Article ID 103087, 2019.

[24] S. Jafari, H. Derakhshankhah, L. Alaei, A. Fattahi, B. S. Varnamkhasti, and A. A. Saboury, "Mesoporous silica nanoparticles for therapeutic/diagnostic applications," *Biomed. Pharmacother*, vol. 109, pp. 1100–1111, 2019.

[25] Q. Zhao, Y. Lin, N. Han et al., "Mesoporous carbon nanomaterials in drug delivery and biomedical application," *Drug Delivery*, vol. 24, no. 2, pp. 94–107, 2017.

[26] K. Chen and S. Mitra, "Incorporation of functionalized carbon nanotubes into hydrophobic drug crystals for enhancing aqueous dissolution," *Colloids Surfaces B Biointerfaces*, vol. 173, pp. 386–391, 2019.

[27] S. Mallakpour and L. khodadadzadeh, "Ultrasonic-assisted fabrication of starch/MWCNT-glucose nanocomposites for drug delivery," *Ultrasonics Sonochemistry*, vol. 40, pp. 402–409, 2018.

[28] A. V. V. V. Ravi Kiran, G. Kusuma Kumari, and P. T. Krishnamurthy, "Carbon nanotubes in drug delivery: focus on anticancer therapies," *Journal of Drug Delivery Science and Technology*, vol. 59, Article ID 101892, 2020.

[29] M. Toński, J. Dołżonek, M. Paszkiewicz, J. Wojsławski, P. Stepnowski, and A. Białk-Bielińska, "Preliminary evaluation of the application of carbon nanotubes as potential adsorbents for the elimination of selected anticancer drugs from water matrices," *Chemosphere*, vol. 201, pp. 32–40, 2018.

[30] S. Saadallah, A. Cable, S. Hamamda et al., "Structural and thermal characterization of multiwall carbon nanotubes (MWCNTs)/aluminum (Al) nanocomposites," *Composites Part B: Engineering*, vol. 151, pp. 232–236, 2018.

[31] S. Begum, H. Ullah, A. Kausar, and M. Siddiq, "Fabrication of epoxy functionalized MWCNTs reinforced PVDF nanocomposites with high dielectric permittivity , low dielectric loss and high electrical conductivity," *Composites Science and Technology*, vol. 167, pp. 497–506, 2018.

[32] A. B. Kanagaraj, P. Chaturvedi, T. Saif Alkindi et al., "Mechanical, thermal and electrical properties of LiFePO4/ MWCNTs composite electrodes," *Materials Letter*, vol. 230, pp. 57–60, 2018.

[33] P. C. Mahakul, K. Sa, B. Das, and P. Mahanandia, "Structural investigation of the enhanced electrical , optical and electrochemical properties of MWCNT incorporated Poly [3-hexylthiophene-2 , 5-diyl] composites," *Materials Chemistry and Physics*, vol. 199, pp. 477–484, 2017.

[34] R. Benlikaya, P. Slobodian, K. Proisl, and I. Morozov, Ascertaining the factors that in fluence the vapor sensor response: the entire case of MWCNT network sensor," *Sensors and Actuators B: Chemical*, vol. 283, pp. 478–486, 2019.

[35] M. Narjinary, P. Rana, A. Sen, and M. Pal, "Enhanced and selective acetone sensing properties of SnO2 -MWCNT nanocomposites: promising materials for diabetes sensor," *Journal of Materials and Design*, vol. 115, pp. 158–164, 2017.

[36] S. Karimi, H. Ghourchian, and A. Banaei, "Protein structure preservation by MWCNTs/RTIL nano-composite," *International Journal of Biological Macromolecules*, vol. 56, pp. 169–174, 2013.

[37] M. Gajendiran, S. J. Kim, J. Choi, and K. Kim, "Conductive biomaterials for tissue engineering applications," *Journal of Industrial and Engineering Chemistry*, vol. 51, pp. 12–26, 2017.

[38] S. Gholizadeh, F. Moztarzadeh, N. Haghighipour, and Z. Allahyari, "Preparation and characterization of novel functionalized multiwalled carbon nanotubes/chitosan/βL -Glycerophosphate scaffolds for bone tissue engineering," *International Journal of Biol. Macromolecules*, vol. 97, pp. 365–372, 2017.

[39] S. A. X. Stango and U. Vijayalakshmi, "Synthesis and characterization of hydroxyapatite/carboxylic acid functionalized MWCNTS composites and its triple layer coatings for biomedical applications," *Ceramics International*, vol. 45, no. 1, pp. 69–81, 2019.

[40] Y. Wang, Y. Jin, W. Chen et al., "Construction of nanomaterials with targeting phototherapy properties to inhibit resistant bacteria and biofilm infections," *Chemical Engineering Journal*, vol. 358, pp. 74–90, 2019.

[41] M. A. Saleemi, Y. L. Kong, P. V. C. Yong, and E. H. Wong, "An overview of recent development in therapeutic drug carrier system using carbon nanotubes," *Journal of Drug Delivery Science and Technology*, vol. 59, Article ID 101855, 2020.

[42] Z. Nissar, A. Kazi, M. Safiulla, and M. Faisal, "A thorough study: in-situ aluminium LM6 metal matrix composites reinforced with iron oxide and MWCNTs," *Materials Today Proceedings*, vol. 4, no. 11, pp. 11999–12006, 2017.

[43] H. Kafa, J. T. W. Wang, N. Rubio et al., "The interaction of carbon nanotubes with an invitro blood-brain barrier model and mouse brain invivo," *Biomaterials*, vol. 53, pp. 437–452, 2015.

[44] Y. Peng, L. Chen, S. Ye et al., "Research and development of drug delivery systems based on drug transporter and nanoformulation," *Asian Journal of Pharmaceutical Science*, vol. 15, no. 2, pp. 220–236, 2020.

[45] N. K. Mehra, A. K. Verma, P. R. Mishra, and N. K. Jain, "The cancer targeting potential of d-α-tocopheryl polyethylene glycol 1000 succinate tethered multi walled carbon nanotubes," *Biomaterials*, vol. 35, no. 15, pp. 4573–4588, 2014.

[46] P. S. Uttekar, S. H. Lakade, V. K. Beldar, and M. T. Harde, "Facile synthesis of multi-walled carbon nanotube via folic acid grafted nanoparticle for precise delivery of doxorubicin," *IET Nanobiotechnology*, vol. 13, no. 7, pp. 688–696, 2019.

[47] A. Avcı, İ. İnci, and N. Baylan, "Adsorption of ciprofloxacin hydrochloride on multiwall carbon nanotube," *Journal of Molecular Structure*, vol. 1206, Article ID 127711, 2020.

[48] T. Guo, J. Wu, H. Gao, and Y. Chen, "Covalent functionalization of multi-walled carbon nanotubes with spiropyran for high solubility both in water and in non-aqueous solvents," *Inorganic Chemistry Communications*, vol. 83, pp. 31–35, 2017.

[49] S. Alharthi and Z. El Rassi, "Talanta CE with multi-walled carbon nanotubes (MWCNTs). Part II SDS coated functionalized MWCNTs as pseudo-stationary phases in nanoparticle EKC—Retention behaviors of small and large solutes," *Talanta*, vol. 192, pp. 545–552, 2019.

[50] L. Yien, N. M. Mubarak, L. Sie, C. Han, M. Khalid, and E. C. Abdullah, "Journal of environmental chemical engineering comparative study of acid functionalization of carbon nanotube via ultrasonic and reflux mechanism," *Journal of Environmental Chemical Engineering*, vol. 6, no. 5, pp. 5889–5896, 2018.

[51] W. Zhang, Z. Zhang, and Y. Zhang, "The application of carbon nanotubes in target drug delivery systems for cancer therapies," *Nanoscale Research Letters*, vol. 6, no. 1, p. 555, 2011.

[52] L. Wei, T. Hong, X. Li, M. Li, Q. Zhang, and T. Chen, "New insights into the adsorption behavior and mechanism of alginic acid onto struvite crystals," *Chemical Engineering Journals*, vol. 358, pp. 1074–1082, 2019.

[53] Z. Movasaghi, B. Yan, and C. Niu, "Industrial crops & products adsorption of ciprofloxacin from water by pretreated oat hulls: equilibrium , kinetic , and thermodynamic studies," *Industrial Crop and Products*, vol. 127, pp. 237–250, 2019.

[54] P. Maneechakr and S. Karnjanakom, "Adsorption behaviour of Fe (II) and Cr (VI) on activated carbon: surface chemistry , isotherm , kinetic and thermodynamic studies," *Journal of Chemical Thermodynamics*, vol. 106, pp. 104–112, 2017.

[55] E. Binaeian and A. Heydarinasab, "Adsorption of BSA onto hexagonal mesoporous silicate loaded by APTES and tannin: isotherm , thermodynamic and kinetic studies," *Advanced Powder Technology*, vol. 29, no. 7, pp. 1664–1675, 2018.

[56] S. Wang, L. J. Kong, J. Y. Long, and M. H. Su, "Chemosphere adsorption of phosphorus by calcium- fl our biochar: isotherm , kinetic and transformation studies," *Chemosphere*, vol. 195, pp. 666–672, 2018.

[57] S. Benkaddour, R. Slimani, H. Hiyanae et al., "Removal of reactive yellow 145 by adsorption onto treated watermelon seeds: kinetic and isotherm studies," *Sustainable Chemistry and Pharmacy*, vol. 10, pp. 16–21, 2018.

[58] Y. Kim and J. Kim, "Isotherm , kinetic and thermodynamic studies on the adsorption of paclitaxel onto sylopute," *Journal of Chemical Thermodynamics*, vol. 130, pp. 104–113, 2019.

[59] D. Nara, S. Insa, A. A. Mozeto, M. Petrovic, T. F. Chaves, and P. S. Fadini, "Chemosphere equilibrium and kinetic studies of the adsorption of antibiotics from aqueous solutions onto powdered zeolites," *Chemosphere*, vol. 205, pp. 137–146, 2018.

[60] Q. Wang, X. Q. Jin, J. H. Sun, S. Y. Bai, and X. Wu, "PAA-grafted surface and fractal feature of dense nanosilica spheres

for ibuprofen delivery," *Materials Chemistry and Physics*, vol. 195, pp. 213–223, 2017.

[61] A. Tamayo, M. A. Mazo, M. D. Veiga, R. Ruiz-caro, F. Notario-pérez, and J. Rubio, "Drug kinetics release from eudragit—tenofovir @ SiOC tablets," *Materials Science Engineering C*, vol. 75, pp. 1097–1105, 2017.

[62] M. Shafiee, R. Foroutan, K. Fouladi, M. Ahmadlouydarab, and B. Ramavandi, "Application of oak powder/Fe 3O4 magnetic composite in toxic metals removal from aqueous solutions," *Advanced Powder Technology*, vol. 30, 2018.

[63] A. V. Dolganov, E. E. Muryumin, O. Y. Chernyaeva, E. A. Chugunova, V. P. Mishkin, and K. N. Nishcev, "Fabrication of new metal-free materials for the hydrogen evolution reaction on base of the acridine derivatives immobilized on carbon materials," *Materials Chemistry and Physics*, vol. 224, pp. 148–155, 2019.

[64] H. S. Shin and J. H. Kim, "Isotherm, kinetic and thermodynamic characteristics of adsorption of paclitaxel onto Diaion HP-20," *Process Biochemistry*, vol. 51, no. 7, pp. 917–924, 2016.

[65] J. Qian, M. Shen, P. Wang et al., "Perfluorooctane sulfonate adsorption on powder activated carbon: effect of phosphate (P) competition, pH, and temperature," *Chemosphere*, vol. 182, pp. 215–222, 2017.

[66] H. M. Jang, S. Yoo, Y. K. Choi, S. Park, and E. Kan, "Adsorption isotherm, kinetic modeling and mechanism of tetracycline on pinus taeda-derived activated biochar," *Bioresource Technology*, vol. 259, pp. 24–31, 2018.

[67] S. M. Mirsoleimani-Azizi, P. Setoodeh, S. Zeinali, and M. R. Rahimpour, "Tetracycline antibiotic removal from aqueous solutions by MOF-5: adsorption isotherm, kinetic and thermodynamic studies," *Journal of Environmental Chemical Engineering*, vol. 6, no. 5, pp. 6118–6130, 2018.

[68] N. Deihimi, M. Irannajad, and B. Rezai, "Equilibrium and kinetic studies of ferricyanide adsorption from aqueous solution by activated red mud," *Journal of Environmental Management*, vol. 227, pp. 277–285, 2018.

[69] C. Boehler, C. Kleber, N. Martini et al., "Actively controlled release of dexamethasone from neural microelectrodes in a chronic in vivo study," *Biomaterials*, vol. 129, pp. 176–187, 2017.

[70] E. Khodaverdi, F. Kheirandish, F. S. Mirzazadeh Tekie, B. Z. Khashyarmanesh, F. Hadizadeh, and H. Moallemzadeh Haghighi, "Preparation of a sustained release drug delivery system for dexamethasone by a thermosensitive, in situ forming hydrogel for use in differentiation of dental pulp," *ISRN Pharmaceutics*, vol. 2013, Article ID 983053, 6 pages, 2013.

[71] X. Luo, C. Matranga, S. Tan, N. Alba, and X. T. Cui, "Carbon nanotube nanoreservior for controlled release of anti-inflammatory dexamethasone," *Biomaterials*, vol. 32, no. 26, pp. 6316–6323, 2011.

[72] P. P. Komane, P. Kumar, T. Marimuthu et al., "Dexamethasone-loaded, pegylated, vertically aligned, multiwalled carbon nanotubes for potential ischemic stroke intervention," *Molecules*, vol. 23, p. 6, 2018.